

Subwavelength angle-sensing photodetectors inspired by directional hearing in small animals

Soongyu Yi¹, Ming Zhou¹, Zongfu Yu¹, Pengyu Fan², Nader Behdad¹, Dianmin Lin^{2,3}, Ken Xingze Wang⁴, Shanhui Fan^{3,4} and Mark Brongersma^{2*}

Sensing the direction of sounds gives animals clear evolutionary advantage. For large animals, with an ear-to-ear spacing that exceeds audible sound wavelengths, directional sensing is simply accomplished by recognizing the intensity and time differences of a wave impinging on its two ears¹. Recent research suggests that in smaller, subwavelength animals, angle sensing can instead rely on a coherent coupling of soundwaves between the two ears^{2–4}. Inspired by this natural design, here we show a subwavelength photodetection pixel that can measure both the intensity and incident angle of light. It relies on an electrical isolation and optical coupling of two closely spaced Si nanowires that support optical Mie resonances^{5–7}. When these resonators scatter light into the same free-space optical modes, a non-Hermitian coupling results that affords highly sensitive angle determination. By straightforward photocurrent measurements, we can independently quantify the stored optical energy in each nanowire and relate the difference in the stored energy between the wires to the incident angle of a light wave. We exploit this effect to fabricate a subwavelength angle-sensitive pixel with angular sensitivity, $\delta\theta = 0.32^\circ$.

The pixels in a conventional imaging chip detect only the intensity of light, and all phase information is lost. While the intensity information alone is sufficient for traditional applications, such as photography, this limitation becomes apparent in advanced imaging tasks. For example, a light field camera can use information from different incident angles to refocus an image even after it is taken^{8–10}. A measurement of the incident angle is typically achieved by combining bulky optical components such as lenses or gratings with photodetecting pixels. These elements are expensive to assemble, and only recently have angle-sensitive pixels successfully been integrated into a CMOS architecture^{11,12}. Their minimum size was limited to several micrometres, as their operation relies on the use of multi-period gratings. With current scaling trends for imaging systems, the size of pixels is rapidly approaching the optical wavelength λ_0 . This has prompted the intriguing question of whether angle-sensing pixels can be realized at this length scale or even below. Approaches based on conventional optical elements cannot be miniaturized indefinitely because diffraction results in a decrease in accuracy. Figure 1a illustrates this point for a lens-based system in which the incident angle θ is measured by focusing light from different directions to distinct spatial locations. The measurement accuracy is reduced by the diffraction-limited spot size in the focus, which scales inversely with the lens diameter d as $\Delta\theta \sim \lambda_0/d\cos\theta$ (Supplementary Section 1). Consequently, when d falls below λ_0 ,

the accuracy degrades severely. This accuracy can be quantified in terms of a minimum detectable angle change $\delta\theta$ that is ultimately limited by the presence of noise.

The directional sensing of sounds for small animals with two independent ears is also fundamentally limited. The interaural time difference for the arrival of sound waves simply becomes too small to detect directly from the timing between neural spikes¹³, and the interaural intensity difference diminishes as the shadow of a sub-wavelength body is blurred by wave diffraction. Instead, some animals rely on acoustic coupling of their ears to achieve directional hearing. For example, the gecko uses a tunnel through the head to acoustically couple its eardrums (Fig. 1b)^{14,15}. Acoustic simulations suggest that this coupling greatly amplifies interaural differences^{16,17}.

Our proposed optical analogue for the small animal auditory system consists of two closely spaced Si nanowires serving as optical resonators (Fig. 2a). We use coupled mode theory to model the signal amplitudes $a_{1,2}$ initially assuming that each wire supports single resonant modes that are coupled to the free-space continuum as^{18–20}

$$i \frac{d}{dt} \begin{pmatrix} a_1 \\ a_2 \end{pmatrix} = H_0 \begin{pmatrix} a_1 \\ a_2 \end{pmatrix} + H_i \begin{pmatrix} a_1 \\ a_2 \end{pmatrix} + i\kappa_\theta S(\theta) \begin{pmatrix} \exp(-i\pi \sin(\theta) d / \lambda) \\ \exp(i\pi \sin(\theta) d / \lambda) \end{pmatrix} \quad (1)$$

where $|a_{1,2}|^2$ is normalized to represent the stored energy in the resonators. $H_0 = \begin{pmatrix} \omega_0 - i\gamma & 0 \\ 0 & \omega_0 - i\gamma \end{pmatrix}$ is the usual Hamiltonian for a pair of two independent resonators, with ω_0 and γ being the resonant frequency and the decay rate, respectively. The non-Hermitian Hamiltonian $H_i = \begin{pmatrix} 0 & \gamma_c \\ \gamma_c & 0 \end{pmatrix}$ treats the far-field coupling of the resonators via the radiation continuum (that is open, leakage channels). The coupling strength is quantified by $\gamma_c = \gamma_r + i\gamma_i$, where γ_r and γ_i describe the real and imaginary part of the coupling strength. The magnitude of γ_r quantifies the exchange of virtual photons²¹, that is, energy that does not escape to the far-field or reactive power. The imaginary part γ_i quantifies the radiation leakage from the resonators into the same optical mode(s) of the continuum for this open system²². This type of coupling is also at the origin of super- and sub-radiance seen for a collection of quantum emitters and conceptually linked to constructive or destructive interference of the radiation from the emitters/resonators in the far-field²³. This non-Hermitian coupling makes it possible for the angle of the incident

¹Department of Electrical and Computer Engineering, University of Wisconsin, Madison, WI, USA. ²Geballe Laboratory for Advanced Materials, Stanford, CA, USA. ³Department of Electrical Engineering, Stanford University, Stanford, CA, USA. ⁴Ginzton Laboratory, Stanford University, Stanford, CA, USA.

*e-mail: brongersma@stanford.edu

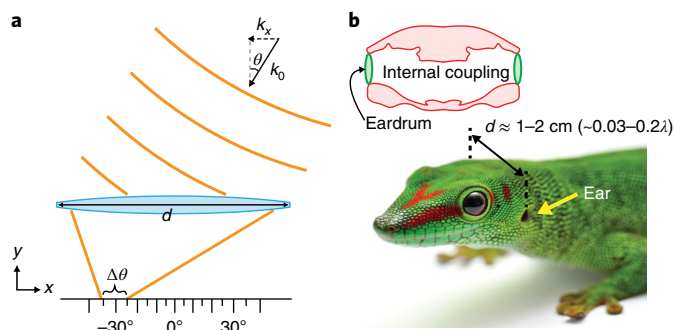


Fig. 1 | Angle sensing in optics using a lens and the internally coupled ears of a small animal. **a**, Concept of incident angle detection using a lens with a diameter d that produces a finite-sized spot in its focal plane with illumination with an off-axis, collimated beam. The angular spread $\Delta\theta$ resulting from diffraction limits the minimum detectable angle change given a limited signal-to-noise ratio (SNR) in a real optical measurement. **b**, Head structure of a gecko showing internal coupling between two eardrums. The distance d between two ears is typically 1–2 cm for most lizards and thus on a subwavelength scale with respect to audible sound wavelengths (8.5–34 cm)¹⁴. Credit: marima/Shutterstock.com

light to manipulate the local energy storage in the resonators and at a deep subwavelength scale. It does so by pumping energy into the two resonators with a flux $S(\theta)$ and coupling rate κ_θ . The angle comes in as it controls the phase $\mp \frac{ix \sin(\theta) d}{\lambda}$ of the excitation wave at the locations of each resonator. When two resonators are far away from each other ($d \gg \lambda_0$), there is no far-field coupling ($\gamma_c = 0$) and the phase of the excitation wave does not impact the energy distribution in the wires. As a result, the energies in the two resonators are always the same—that is, $|a_1|^2 = |a_2|^2$, regardless of the incident angle (black line in Fig. 2b). In contrast, when the resonator spacing is reduced to $d \leq \lambda_0$, there is a non-Hermitian coupling $\gamma_c \neq 0$, resulting in a strong angular response to the incident light (red line in Fig. 2b). The ratio of the amplitudes in the two resonators provides an unambiguous way to determine the incident angle. The angular response is a result of coherent superposition of super- and sub-radiant modes, which is explained in more details in Supplementary Section 2. Without resonance, angle sensing does not work (Supplementary Section 3).

We implemented the direction-sensing pixel using two Si nanowires on a SiO₂ substrate, as schematically shown in Fig. 2c. Both the width and height of the nanowires are 100 nm. Despite their subwavelength size, each wire supports several resonances in the visible spectral regime^{5,6,24,25}. The field profiles for the transverse magnetic (TM, with magnetic field transverse to the nanowire axis) and transverse electric (TE, with electric field transverse to the nanowire axis) resonances are shown in Supplementary Section 5. Whereas the example above describes the simplified case where each nanowire supports a single mode at the illumination frequency, it is important to note that some modes can be doubly degenerate. In those cases, coupled mode theory needs to include four modes (Supplementary Section 6).

Using full-wave simulations of Maxwell's equations, we examined how the light absorption in the nanowires changes with illumination direction. The local absorption in the nanowires is calculated by computing $\sigma(\omega) |E|^2$, where $\sigma(\omega)$ is the conductivity at the angular frequency ω and E is the electric field. The illumination wavelength is fixed at 550 nm, with the incident electric field polarized along the nanowire, causing excitation of the doubly degenerate, second-order TM₂ mode. We first set the spacing to be 100 nm, for which strong coupling is expected. Indeed, the absorption

difference shows a strong angular dependence (red line in Fig. 2d). The maximum contrast ratio for the absorption is around 3. Figure 3a shows the spatial distribution of the absorption for different incident angles. The bright red (dark blue) colour indicates strong (weak) absorption. Under normal incidence at $\theta = 0^\circ$, the two nanowires display identical absorption profiles. The flow of light changes to concentrate more light in one wire when the incident angle is tilted away from the normal. Figure 2c shows the calculated flow lines of the Poynting vector (black lines) to illustrate the flow of light when light is incident from the left at a 45° angle. The resonator on the left effectively casts a shadow and reduces the absorption in the other wire. The extent of the shadow, quantified by the absorption cross-section, can often be much larger than the resonator's geometrical size²⁶. This mechanism of angle sensing is substantially different from that used in radiofrequency direction finding (for more discussion see Supplementary Section 7).

For a larger spacing ($d = 2 \mu\text{m}$), the coupling γ_c is eliminated and no absorption difference between the wires is observed at any incident angle (black line in Fig. 2d). Figure 3d shows how the larger spacing results in the same absorption $\sigma(\omega) |E|^2$ profile in each resonator, irrespective of the incident angle.

Figure 4a presents a schematic of a fabricated device. Gold electrodes cover the ends of each nanowire to form two photodetectors. These photodetectors are electrically isolated from each other, but optically coupled. The difference in photocurrent from each wire is proportional to the difference in light absorption. Figure 4b shows a scanning electron microscope (SEM) image of the device. The inset shows a close-up view of the nanowires (see Supplementary Section 8 for nanowires with shorter length). Each nanowire forms a photoconductive detector whose resistance changes on illumination. The voltage–current relation shows good ohmic contacts (Supplementary Fig. 16). To characterize the optical resonances supported by the wires, we measured responsivity spectra (Fig. 4c,d) using normally incident light and for TM and TE polarization. The spectra show enhanced absorption near the TM₂ and TE₁ resonance wavelengths, where the subscripts label the order number of the resonance as determined by the number of field antinodes. The field distributions for these resonances are shown as insets. The responsivity of the nanowires is discussed further in Supplementary Section 9.

We measured the angular response at a wavelength of 550 nm. For TM polarization, the photocurrent ratio increases from 1 to 3 as the incident angle increases from 0° to 70° (Fig. 4e). For TE polarization, the photocurrent ratio increases monotonically up to 45° (Fig. 4f). In both cases, the experimental results agree well with the full-wave simulations (solid lines in Fig. 4e,f). The peak in Fig. 4f is created by the unique radiation profile of the TE superradiant eigenstate (for a detailed explanation see Supplementary Section 11). This detector can work for unpolarized light by confining the field of view (FOV) to $\pm 45^\circ$, which is sufficient for many applications.

One immediate application of angular photodetectors is triangulation. As a demonstration, we used two angle-sensing photodetectors to triangulate the position of a light-emitting diode (LED). A top-view photograph of the experimental set-up is shown in Fig. 5a. This shows the photodetectors and LED placed in the same horizontal plane. The LED light source has a centre wavelength of 520 nm. A chopper is used together with a lock-in amplifier to measure the photocurrent. Two angle-sensing detectors are mounted on two chips separated by 50 mm. A top-view schematic is shown in Fig. 5b. All coordinates are in millimetres. Using triangulation, the location of the LED during movement, including both the lateral position x and depth y , can be obtained.

In the experiment, we first characterized the angular response of an individual angle-sensing photodetector under LED illumination up to angles of $\pm 30^\circ$. A monotonic angular profile was obtained (red line in Fig. 5c), in agreement with the full-wave simulation results

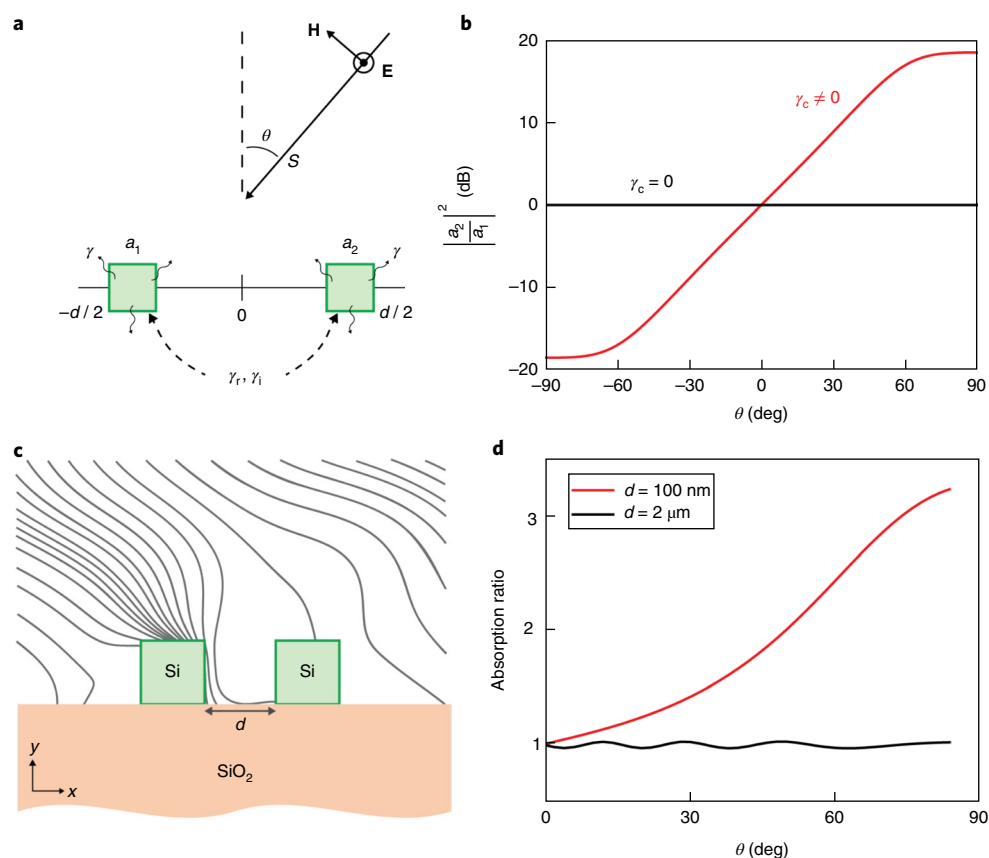


Fig. 2 | Coupled mode theory for a pair of optical Mie resonators used for directional sensing. **a**, Schematic of coupled mode theory for two resonators with amplitudes a_1 and a_2 separated by a distance d . S , γ_i and γ_r quantify the power of the incident light, and the imaginary and real parts of the coupling strength, respectively. γ is the decay rate. H , magnetic field; E , electric field. **b**, Ratio of stored energy in the two resonators. This strongly depends on the incident angle for the coupled case (red line), whereas it remains at 1 for decoupled resonators (black line). $d = 0.05\lambda_0$ and $\gamma = 0.01\omega_0$ are used for both $\gamma_c = 0$ and $\gamma_c \neq 0$ cases. $\gamma_c = 9.8 \times 10^{-3}\omega_0$ is used for the $\gamma_c \neq 0$ case. The effects of spacing d and optical absorption γ_a are discussed in Supplementary Section 4. **c**, Cross-sectional view of two Si nanowires on a SiO_2 substrate with Poynting flux lines for a 45° incident angle θ . **d**, Absorption ratio between two Si nanowires for $d = 100$ nm (red) and $d = 2$ μm (black) as a function of incident angle. In **c, d**, the electric field of the incident wave is along the z direction (TM polarization).

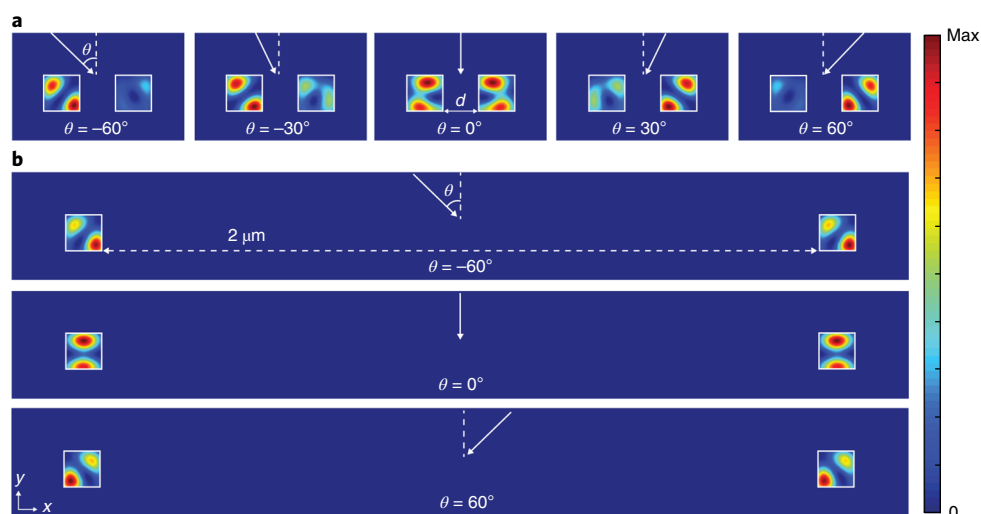


Fig. 3 | Absorption profiles for a coupled and uncoupled pair of Si nanowires for different incident angles. **a**, Absorption profile $\sigma(\omega) |E|^2$ for different incident angles, normalized by the highest absorption density in each case. When $d = 100$ nm, the absorption ratio change between two nanowires is clearly visible for different incident angles. **b**, When $d = 2$ μm, both nanowires feature an almost identical absorption profile for any incident angle. In **a** and **b**, the electric field of the incident wave is along the z direction (TM polarization).

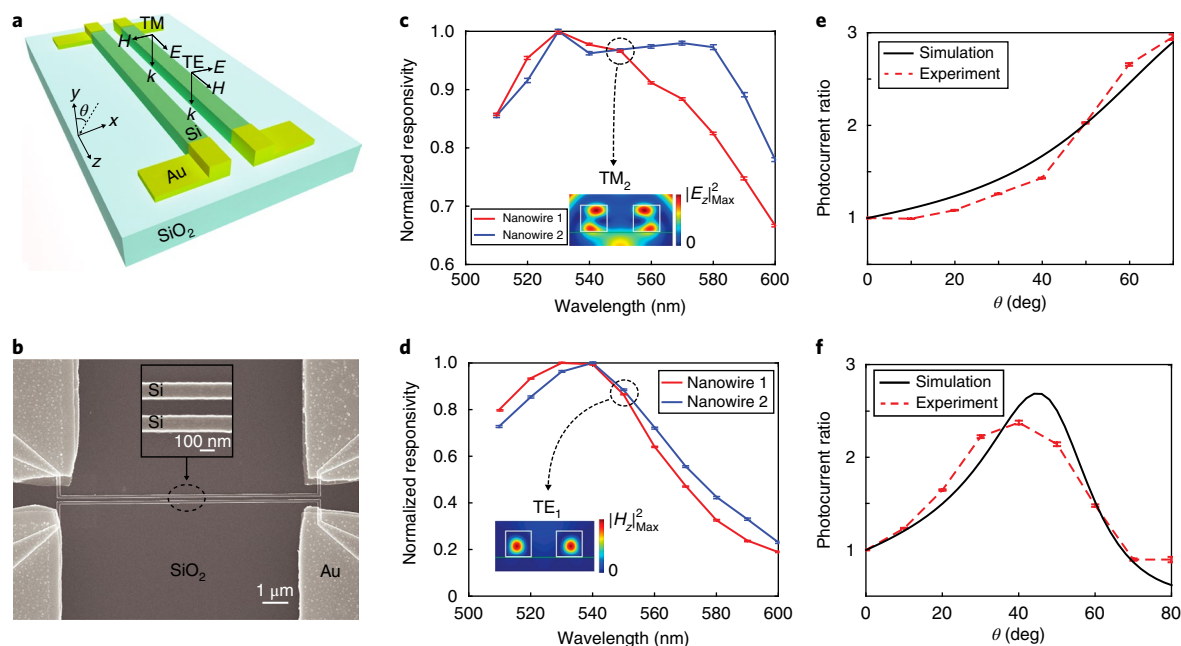


Fig. 4 | Fabrication and performance of the proposed angle-sensing photodetector. **a**, Schematic of an angle-sensing photodetector with two Si nanowires (green) connected with Au (yellow) contacts. **b**, SEM image of a fabricated device. Inset, Close-up view of the two Si wires where the width and the gap between them are all 105 nm. Fabrication tolerance is discussed in Supplementary Section 10. **c,d**, Spectral dependence of the responsivity of the two wires taken with TM (**c**) and TE (**d**) polarized light. This was normalized to the maximum value. Insets, Electric (magnetic) field intensities for the TM_2 (TE_1) resonance. The responsivity is defined as $R = I/P$, where I is the measured photocurrent and P is the incident power on the wire surface. **e**, Angle dependence of the photocurrent ratio in the two wires, measured at a wavelength of 550 nm with the same polarization as in **c**. **f**, Photocurrent ratio for the two nanowires as a function of θ with the same polarization as in **d**.

(black line in Fig. 5c) for unpolarized light. Using the experimental curve as the calibration, we measure the incident angles $\theta_{1,2}$ of the light and then used trigonometry to estimate the location of the LED (Supplementary Section 12). Black markers in Fig. 5b show the calculated LED positions, and red markers show the true locations. The triangulation provides an excellent measurement of the location of the light source.

Compared to existing depth sensing methods based on time-of-flight or stereo cameras²⁷, angular photodetectors provide a much simpler solution to depth sensing. This can reach centimetre accuracy for a range up to 10 m (see Supplementary Section 13 for the calculation), which is comparable to leading commercial depth sensors²⁸. More importantly, it does not use any lenses or require time synchronization.

The minimum detectable angle change is determined by the contrast ratio for the photocurrent as well as the signal-to-noise ratio (SNR) of the photodetector. For near-normal incidence, the minimum detectable angle change can be calculated as $\delta\theta = \frac{2}{\text{SNR}} \frac{\theta_{\max}}{R_{\max} - 1}$ assuming a linear angular dependence that has a dynamic range up to θ_{\max} and a maximum contrast ratio of R_{\max} (see derivation in Supplementary Section 14). In our measurement, we obtained a maximum SNR of 28 dB by using a lock-in amplifier and averaging over multiple measurements. This SNR leads to a $\delta\theta$ of 0.32° . Our detectors are photoconductors, which are known to have high noise levels. Future experiments could employ photodiodes together with integrated amplification circuits to greatly reduce noise. For example, using CMOS image sensing technology, a typical SNR of 43.4 dB (as in ref. ²⁹) can be reached and this leads to a $\delta\theta$ of 0.009° .

Because the geometry of the two nanowires is a faithful imitation of the coupled ears of small animals, it also inherits the same limitations found in the biological world, including a limited operational bandwidth, lack of full azimuth and elevation angle capability, and a difficulty in differentiating multiple incoming waves. The

limitations of these natural designs can be overcome. For example, by using two pairs of angle detectors orientated orthogonally, one can detect both azimuth and elevation angles (Supplementary Section 15). One can also use multiple (instead of two) resonant detectors to expand the bandwidth of operation and to differentiate multiple incident waves. When densely fabricated in arrays, these resonance-based angle sensors also need to be spaced by a minimum distance to avoid inter-pixel coupling, an effect that is further discussed in Supplementary Section 16.

With this newly accessible information about the intrinsic properties of light, angle-sensing pixels can be created for imaging chips that enable a wide variety of new applications for advanced light sensing. For example, the angular information of light may provide better scene awareness for autonomous vehicles and in robotics. Furthermore, electrically isolated and optically coupled photodetectors could further be made to perform multimodal sensing for polarization and wavelength. These light sensors extract highly specific information from the environment and could become pervasive in next-generation smart optoelectronic and artificial intelligence systems.

Online content

Any methods, additional references, Nature Research reporting summaries, source data, statements of data availability and associated accession codes are available at <https://doi.org/10.1038/s41565-018-0278-9>

Received: 22 May 2017; Accepted: 14 September 2018;

Published online: 29 October 2018

References

- Grothe, B., Pecka, M. & McAlpine, D. Mechanisms of sound localization in mammals. *Physiol. Rev.* **90**, 983–1012 (2010).

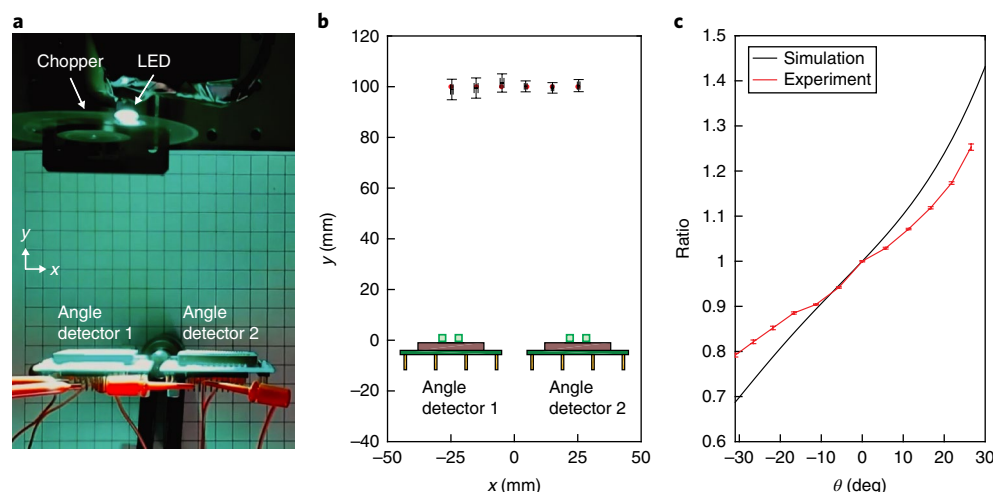


Fig. 5 | Measurement set-up and experimental results for lens-less positioning. **a**, Two angle-sensing detectors mounted on two separate chips are placed 50 mm away from each other in the x direction. An LED light source embedded in a hemispherical glass lens with a diameter of 5.6 mm is placed 100 mm away in the y direction from two angle-sensing detectors. A chopper and a lock-in amplifier is used to measure the photocurrent of nanowires in two angle-sensing detectors. Measurements are carried out at six different LED locations separated 1 cm equally from neighbouring locations. Grid paper with 1 cm squares is placed on the bottom as a scale. **b**, LED position uncertainty in the x and y directions for six discrete measurements in the 2D plane, where the red dots represent the true location of the LED light source. Error bars are generated using 50 measurements at each location with a propagation of uncertainty method. The LED is assumed to be a point source for calculations. **c**, Full-wave simulation and experimentally measured photocurrent ratio under unpolarized light. Error bars were generated based on 100 measurements in each location. The average length of the error bars is 0.006.

- Chung, S.-H., Pettigrew, A. & Anson, M. Dynamics of the amphibian middle ear. *Nature* **272**, 142–147 (1978).
- Miles, R. N., Robert, D. & Hoy, R. R. Mechanically coupled ears for directional hearing in the parasitoid fly *Ormiaochracea*. *J. Acoust. Soc. Am.* **98**, 3059–3070 (1995).
- Römer, H. & Schmidt, A. K. D. Directional hearing in insects with internally coupled ears. *Biol. Cybern.* **110**, 247–254 (2016).
- Mie, G. Beiträge zur Optik trüber Medien, speziell kolloidaler Metallösungen. *Ann. Phys.* **330**, 377–445 (1908).
- Cao, L. et al. Engineering light absorption in semiconductor nanowire devices. *Nat. Mater.* **8**, 643–647 (2009).
- Kuznetsov, A. I., Miroshnichenko, A. E., Brongersma, M. L., Kivshar, Y. S. & Luk'yanchuk, B. Optically resonant dielectric nanostructures. *Science* **354**, 2472 (2016).
- Ng, R. et al. *Light Field Photography with a Hand-Held Plenoptic Camera*, Computer Science Tech Report 2005-02 (Stanford University, 2005).
- Wang, A., Gill, P. & Molnar, A. Light field image sensors based on the Talbot effect. *Appl. Opt.* **48**, 5897–5905 (2009).
- Wang, A. & Molnar, A. A light-field image sensor in 180 nm CMOS. *IEEE J. Solid-State Circuits* **47**, 257–271 (2012).
- Wang, A., Gill, P. & Molnar, A. in *Proceedings of the IEEE Custom Integrated Circuits Conference* 371–374 (IEEE, New York, 2009).
- Sivaramakrishnan, S., Wang, A., Gill, P. R. & Molnar, A. in *Proceedings of the 2011 IEEE International Electronic Devices Meeting* 191–194 (IEEE, New York, 2011).
- Pollack, G. S. Sensory cues for sound localization in the cricket *Teleogryllus oceanicus*: interaural difference in response strength versus interaural latency difference. *J. Comp. Physiol. A* **189**, 143–151 (2003).
- Christensen-Dalsgaard, J. & Manley, G. A. Directionality of the lizard ear. *J. Exp. Biol.* **208**, 1209–1217 (2005).
- Christensen-Dalsgaard, J., Tang, Y. & Carr, C. E. Binaural processing by the gecko auditory periphery. *J. Neurophysiol.* **105**, 1992–2004 (2011).
- Vossen, C., Christensen-Dalsgaard, J. & van Hemmen, J. L. Analytical model of internally coupled ears. *J. Acoust. Soc. Am.* **128**, 909–918 (2010).
- Vedurmudi, A. P. et al. How internally coupled ears generate temporal and amplitude cues for sound localization. *Phys. Rev. Lett.* **116**, 28101 (2016).
- Suh, W., Wang, Z. & Fan, S. Temporal coupled-mode theory and the presence of non-orthogonal modes in lossless multimode cavities. *IEEE J. Quantum Electron.* **40**, 1511–1518 (2004).
- Verslegers, L., Yu, Z., Catrysse, P. B. & Fan, S. Temporal coupled-mode theory for resonant apertures. *J. Opt. Soc. Am. B* **27**, 1947–1956 (2010).
- Verslegers, L., Yu, Z., Ruan, Z., Catrysse, P. B. & Fan, S. From electromagnetically induced transparency to superscattering with a single structure: a coupled-mode theory for doubly resonant structures. *Phys. Rev. Lett.* **108**, 83902 (2012).
- Scully, M. O. Collective Lamb shift in single photon Dicke superradiance. *Phys. Rev. Lett.* **102**, 143601 (2009).
- Zhang, S. et al. Anti-Hermitian plasmon coupling of an array of gold thin-film antennas for controlling light at the nanoscale. *Phys. Rev. Lett.* **109**, 193902 (2012).
- Lyuboshitz, V. L. Resonance interaction between two identical dipole emitters. *Sov. Phys. J. Exp. Theor. Phys.* **26**, 937–942 (1968).
- Brönstrup, G. et al. Optical properties of individual silicon nanowires for photonic devices. *ACS Nano* **4**, 7113–7122 (2010).
- Cao, L., Fan, P. & Brongersma, M. L. Optical coupling of deep-subwavelength semiconductor nanowires. *Nano. Lett.* **11**, 1463–1468 (2011).
- Zhou, M., Shi, L., Zi, J. & Yu, Z. Extraordinarily large optical cross section for localized single nanoresonator. *Phys. Rev. Lett.* **115**, 23903 (2015).
- Besl, P. J. Active, optical range imaging sensors. *Mach. Vis. Appl.* **1**, 127–152 (1988).
- Blais, F. Review of 20 years of range sensor development. *J. Electron. Imaging* **13**, 231–240 (2004).
- Semiconductors Components Industries. VITA 25K Image Sensor Data Sheet NOIV1SN025KA, <http://www.onsemi.com/pub/Collateral/NOIV1SN025KA-D.PDF> (2016).

Acknowledgements

The work at the University of Wisconsin was funded by the Office of Naval Research (N00014-14-1-0300). The work at Stanford was supported by a Multi University Research Initiative (MURIs FA9550-14-1-0389) and an individual investigator grant (FA9550-17-1-0331) from the AFOSR.

Author contributions

M.B. and Z.Y. directed the research. S.Y., M.Z., P.F. and D.L. performed the experiments. S.Y. and K.X.W. performed the simulations. M.Z. developed the analytical theory. All authors were involved in analysing the data and writing the manuscript.

Competing interests

The authors declare no competing interests.

Additional information

Supplementary information is available for this paper at <https://doi.org/10.1038/s41565-018-0278-9>.

Reprints and permissions information is available at www.nature.com/reprints.

Correspondence and requests for materials should be addressed to M.B.

Publisher's note: Springer Nature remains neutral with regard to jurisdictional claims in published maps and institutional affiliations.

© The Author(s), under exclusive licence to Springer Nature Limited 2018

Methods

For the fabrication of the subwavelength angle-sensing photodetector, a lightly n-doped poly-Si was deposited on a SiO₂ substrate using low-pressure chemical vapour deposition (LPCVD). Electron beam lithography was used to define the

nanowires followed by dry etch using a Cr mask to etch down the Si layer and create Si nanowires. Au contacts were made using electron-beam lithography to define the patterns followed by Au deposition using electron-beam physical vapour deposition.

In the format provided by the authors and unedited.

Subwavelength angle-sensing photodetectors inspired by directional hearing in small animals

Soongyu Yi¹, Ming Zhou¹, Zongfu Yu¹, Pengyu Fan², Nader Behdad¹, Dianmin Lin^{2,3},
Ken Xingze Wang⁴, Shanhui Fan^{3,4} and Mark Brongersma^{2*}

¹Department of Electrical and Computer Engineering, University of Wisconsin, Madison, WI, USA. ²Geballe Laboratory for Advanced Materials, Stanford, CA, USA. ³Department of Electrical Engineering, Stanford University, Stanford, CA, USA. ⁴Ginzton Laboratory, Stanford University, Stanford, CA, USA.

*e-mail: brongersma@stanford.edu

Section 1. The role of diffraction in reducing the accuracy of an angle measurement with a finite-sized lens

When an aperture having a finite size is used to focus a beam, light will exhibit diffraction due to the finite size of the lens' aperture. As a result, a focused beam will have a finite spot size that corresponds to a spread in angle ($\Delta\theta$) as seen in Fig. S1.

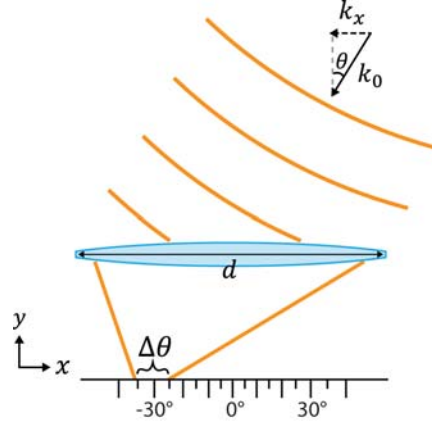


Fig. S1 Schematic of an incident-angle detection scheme using a lens. d is the diameter of the lens and $\Delta\theta$ is limited by the spot size of the focus.

For a lens having a diameter d as in Fig. S1, there will be a spread in the wavenumber in the x-direction due to the finite size of the lens:

$$\Delta k_x = \frac{2\pi}{d} \quad (\text{S1})$$

k_x can be expressed using the free-space wavenumber k_0 and incident angle θ as:

$$k_x = k_0 \sin\theta \quad (\text{S2})$$

The differential form of Eq. S2 with respect to θ can be written as:

$$\Delta k_x = k_0 \cos\theta \Delta\theta \quad (\text{S3})$$

Substituting Δk_x in Eq. S1 into Δk_x in Eq. S3 and replacing k_0 with $2\pi/\lambda_0$ gives:

$$\frac{2\pi}{d} = \frac{2\pi}{\lambda_0} \cos\theta \Delta\theta \quad (\text{S4})$$

Thus, an angular spread $\Delta\theta$ can be expressed as:

$$\Delta\theta = \frac{\lambda_0}{d \cos\theta} \quad (\text{S5})$$

In a real optical measurement, the number of collected photons is limited and this results in a lack of contrast between closely-spaced focal spots produced by incident plane waves with incident angles that differ by $\Delta\theta$. In other words, the angular resolution is limited. Similar arguments led

to the Rayleigh criterion, which states that a lens with an aperture size of d could not differentiate two plane waves if the incident angle difference is less than

$$\Delta\theta = 1.22 \frac{\lambda_0}{d} \quad (\text{S6})$$

Section 2-a. Coupled mode theory describing two single mode resonators

We start by modeling the simple case of two single-mode resonators coupled to the free-space continuum as [1-3]:

$$i \frac{d}{dt} \begin{pmatrix} a_1 \\ a_2 \end{pmatrix} = H_0 \begin{pmatrix} a_1 \\ a_2 \end{pmatrix} + H_i \begin{pmatrix} a_1 \\ a_2 \end{pmatrix} + i\kappa_\theta S(\theta) \begin{pmatrix} \exp(-i\pi \sin(\theta) d/\lambda) \\ \exp(i\pi \sin(\theta) d/\lambda) \end{pmatrix} \quad (\text{S7})$$

where $|a_{1,2}|^2$ is normalized to represent the stored energy in the resonators. $H_0 = \begin{pmatrix} \omega_0 - i\gamma & 0 \\ 0 & \omega_0 - i\gamma \end{pmatrix}$ is the usual Hamiltonian for a pair of two independent resonators with ω_0 and γ being the resonant frequency and the decay rate, respectively. The incident light, whose flux is represented by $S(\theta)$, pumps energy into two resonators with an effectiveness determined by a coupling rate κ_θ . It is important to note that the phases $\mp \frac{i\pi \sin(\theta) d}{\lambda}$ of the excitation wave at the relevant location of each resonator are different because of their spatial separation. A similar coupled mode theory can be derived for coupled acoustic resonators [4] as shown in the SI section 2-e.

We turn our focus to the non-Hermitian Hamiltonian $H_i = \begin{pmatrix} 0 & \gamma_c \\ \gamma_c & 0 \end{pmatrix}$, which facilitates an angularly-dependent response. The coupling strength is quantified by $\gamma_c = \gamma_r + i\gamma_i$, where γ_r and γ_i describe the real and the imaginary part of the coupling strength, respectively (see derivation of real and imaginary part of coupling coefficients in SI section 2-c). The real part γ_r is governed by the exchange of virtual photons [5], while the imaginary part γ_i arises when localized resonators couple to the same optical mode(s) in the continuum in an open system [6], a conceptually similar origin as the super and subradiance seen for a collection of quantum emitters [7-10]. This non-Hermitian coupling allows the incident light to manipulate the local storage of resonant energy at a deep subwavelength scale. For example, Ref [6] shows the spectral resolving capability using non-Hermitian interaction.

Next, we discuss how the imaginary part of the coupling gives rise to an angularly-dependent response. The mathematical framework that leads to Eq. S7 allows for a straightforward calculation of the energy storage in the individual nanowires, which is needed to predict the photocurrent generation in each wire. However, to understand the angle-dependence of the photoresponse, it is more insightful to describe the system in terms the superradiant and subradiant eigenstates supported by the optically-coupled pair of nanowires. We illustrate this point for two electric dipole resonators that oscillate in phase for the even, superradiant eigenstate and 180° out-of-phase for the odd, subradiant eigenstate. The distinct symmetry of these eigenstates naturally gives rise to the different angular radiation patterns shown in Fig. S2. By reciprocity, when light

is incident from different angles, the excitation amplitudes of the super and subradiant are also different. For illumination at normal incidence, only the superradiant eigenstate is excited and thus the two resonators have equal amplitudes. When the incident light tilts away from the normal, the subradiant eigenstate can also be excited. When both even and odd eigenstate are excited simultaneously, their fields amplitude will add constructively in one wire and negate each other in the other wire. In other words, the energy is redistributed between the wires to make the photocurrent generation in one wire more effective. As the odd eigenstate is subradiant and features a higher radiation Q than the even, superradiant eigenstate, the energy storage in this state can become significant with minor tilting of the incident beam. Naively, it is expected that a smaller spacing will give rise to stronger γ_i and thus a greater angular response. However, γ_r also increases with smaller spacing and this coupling cannot be larger than the bandwidth of the resonators to avoid a detrimental splitting of the Eigen-frequencies of the super and subradiant eigenstates. On the other hand, the imaginary part of the coupling never splits the Eigen-frequency and can take any large value.

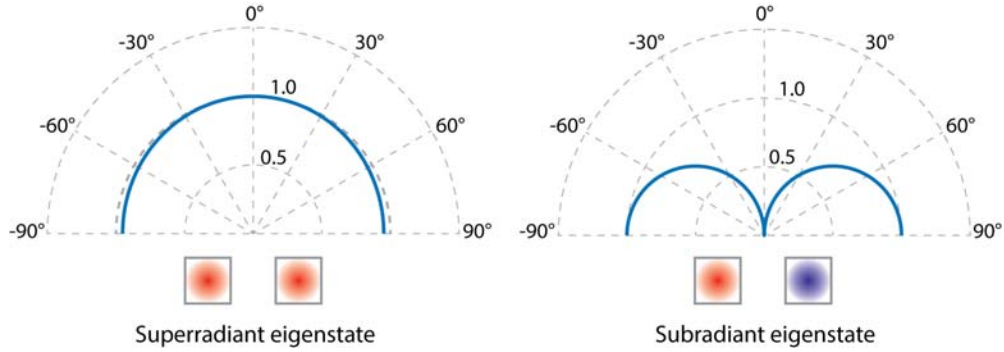


Fig. S2 Example of the angular profile (blue curves) and the phase configuration of the radiation of the super and subradiant eigenstates for the case of electric dipole radiators. Here we assume the spacing between the two is much smaller ($0.1 \lambda_0$) than wavelength. Red and blue are used to indicate a phase difference of π .

Section 2-b. Working principle of an angular sensing capability in coupled resonators

As we discussed in the main text, the non-Hermitian coupling between coupled resonators facilitates angular sensing. In this section, we will discuss the underlying principle in detail using coupled mode theory.

Two resonators coupled to the free-space continuum can be modelled using coupled mode theory as [11-13]

$$i \frac{d}{dt} \begin{pmatrix} a_1 \\ a_2 \end{pmatrix} = \begin{pmatrix} \omega_0 - i\gamma & 0 \\ 0 & \omega_0 - i\gamma \end{pmatrix} \begin{pmatrix} a_1 \\ a_2 \end{pmatrix} + \begin{pmatrix} 0 & \gamma_c \\ \gamma_c & 0 \end{pmatrix} \begin{pmatrix} a_1 \\ a_2 \end{pmatrix} + i\kappa_\theta S(\theta) \begin{pmatrix} \exp(-i\pi \sin(\theta) d/\lambda) \\ \exp(i\pi \sin(\theta) d/\lambda) \end{pmatrix} \quad (\text{S8})$$

where $|a_{1,2}|^2$ is normalized to represent the energy of the resonant modes. ω_0 and γ are the resonant frequency and the decay rate, respectively. The non-Hermitian coupling strength is given by $\gamma_c = \gamma_r + i\gamma_i$, where γ_r and γ_i quantify the strength of the real and the imaginary parts of the coupling strength, respectively. The incident light, whose flux is represented by $S(\theta)$, pumps energy into two resonators with an effectiveness determined by a coupling rate κ_θ . The phases $\mp i\pi \sin(\theta) d/\lambda$ for the two resonators are different based on their spatial separation.

Under a steady-state excitation with an angular frequency of ω , we can elect to write the amplitude for each resonator mode as a superposition of the superradiant and subradiant eigenstates.

$$\begin{pmatrix} a_1 \\ a_2 \end{pmatrix} = \alpha(\omega, \theta) \begin{pmatrix} 1 \\ 1 \end{pmatrix} + \beta(\omega, \theta) \begin{pmatrix} -1 \\ 1 \end{pmatrix} \quad (\text{S9})$$

where $\begin{pmatrix} 1 \\ 1 \end{pmatrix}$ and $\begin{pmatrix} -1 \\ 1 \end{pmatrix}$ represent the in-phase superradiant and out-of-phase subradiant eigenstates, respectively. Here $\alpha(\omega, \theta)$ and $\beta(\omega, \theta)$ are the amplitudes of the in-phase and out-of-phase eigenstates, respectively. They are given by:

$$\alpha(\omega, \theta) = \frac{i\kappa_\theta S(\theta) \cos\left(\frac{\pi \sin(\theta) d}{\lambda}\right)}{\omega - \omega_0 + i\gamma - \gamma_r - i\gamma_i} \quad (\text{S10a})$$

$$\beta(\omega, \theta) = \frac{-\kappa_\theta S(\theta) \sin\left(\frac{\pi \sin(\theta) d}{\lambda}\right)}{\omega - \omega_0 + i\gamma + \gamma_r + i\gamma_i} \quad (\text{S10b})$$

The energy in the two resonators $|a_1|^2$ and $|a_2|^2$ can be written as:

$$|a_1|^2 = |\alpha(\omega, \theta)|^2 + |\beta(\omega, \theta)|^2 - 2|\alpha(\omega, \theta)\beta(\omega, \theta)|\cos(\Delta\phi) \quad (\text{S11a})$$

$$|a_2|^2 = |\alpha(\omega, \theta)|^2 + |\beta(\omega, \theta)|^2 + 2|\alpha(\omega, \theta)\beta(\omega, \theta)|\cos(\Delta\phi) \quad (\text{S11b})$$

Here $\Delta\phi$ is the phase difference between $\alpha(\omega, \theta)$ and $\beta(\omega, \theta)$. When the two resonators are completely decoupled, i.e. $\gamma_r = 0$ and $\gamma_i = 0$, the phase difference between the two eigenstates is always $\Delta\phi = \pi/2$, independent of the excitation frequency (dashed black line in Fig. S3a). This phase difference simply results from having even (cosine-like) and odd (sine-like) modes. Without any form of coupling, this value of $\Delta\phi$ is also independent of the incident angle. Since the energy difference between the resonators is given by $4|\alpha(\omega, \theta)\beta(\omega, \theta)|\cos(\Delta\phi)$, the value of $\Delta\phi = \pi/2$ results in equal stored energy in the two resonators. This is intuitively expected for identical resonators without any type of optical coupling.

On the other hand, when the two resonators are coupled together, the phase difference generally deviates from $\pi/2$. Generally, both real and imaginary parts of coupling are present. In Fig. S3a we show the case where $\gamma_r = -0.5\gamma$ and $\gamma_i = 0.5\gamma$. In contrast to the case without coupling (dashed line), we have a phase difference close to π around the Eigen-frequency, resulting in very strong angular response (See Fig. S3b).

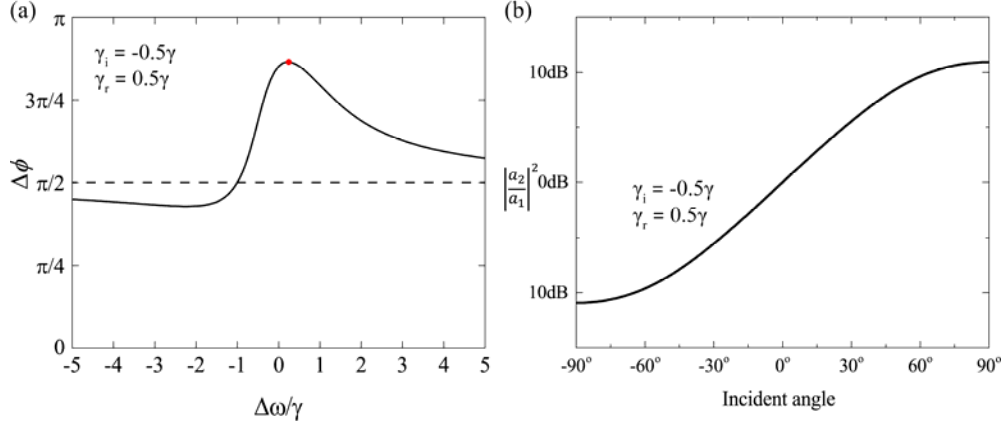


Fig. S3 Phase difference and contrast ratio of two resonators. (a) Phase difference for different amounts of frequency detuning from resonance ($\Delta\omega = \omega - \omega_0$). Here γ is the intrinsic decay rate of an individual resonator. The dashed line indicates the case without coupling, i.e. $\gamma_i = 0$ and $\gamma_r = 0$. The solid line indicates a case with both non-zero real and imaginary parts of the coupling strength, i.e. $\gamma_i = -0.5\gamma$ and $\gamma_r = 0.5\gamma$. (b) Contrast ratio at the maximum phase difference, which is marked in (a) by the red dot. The coupling provides a way to unambiguously determine the incident angle of a light beam.

Next, we elucidate the different ways in which the real and the imaginary parts of the coupling change our ability to determine the angle of an incident beam. This is intimately linked to the way in which the coupling can modify the phase difference between the superradiant and subradiant eigenstates. In general, as the frequency of the excitation wave sweeps across an Eigen-frequency, the phase of the eigenstate incurs a π phase swing, starting from 0 far below the Eigen-frequency, gradually increasing to $\pi/2$ at the Eigen-frequency, and then eventually to π at frequencies far above the Eigen-frequency. As the frequency is increased, the amplitude also changes and reaches a maximum value at the resonant frequency. Figure S4a shows the characteristic phase evolution for the superradiant $\alpha(\omega, \theta)$ and subradiant $\beta(\omega, \theta)$ Eigenstates if we assume no coupling between the resonators, i.e. $|\gamma_i| = |\gamma_r| = 0$. Here, we offset the phase $\alpha(\omega, \theta)$ by $\pi/2$ to emphasize that the phase of $\beta(\omega, \theta)$ progresses in exactly the same manner. This results in a constant phase difference between the two at all frequencies (Fig. S4d). This is expected as both Eigenstates have the same resonant frequency and the same bandwidth. As $\Delta\phi = \pi/2$, each resonator features the same stored energy.

The coupling breaks this constant $\pi/2$ phase difference. In an open system, both the real and the imaginary parts of the coupling are generally non-zero, which makes the system non-Hermitian. To understand their different impact, we first look at the role of the imaginary part of the coupling γ_i by choosing a case where $|\gamma_i| \gg |\gamma_r|$. The imaginary part of the coupling does not break the energy degeneracy between the superradiant and subradiant Eigenstates. However, this coupling does change the bandwidth over which the π phase evolution occurs. The in-phase superradiant eigenstate decays more quickly at the rate $\gamma - \gamma_i$ and shows a faster phase evolution whereas the out-of-phase subradiant eigenstate decays more slowly at the rate $\gamma + \gamma_i$ and displays a slower phase evolution. Note γ_i is mostly negative for deep subwavelength spacing (see Fig. S8a for example). The resulting difference in the phase evolution (Fig. S4b) results in a spectral regime where the phase difference between the two Eigenstates can approach π , or 0 (Fig. S4e). Such

phase differences result in a redistribution of the energy between the resonators and produce an angular response.

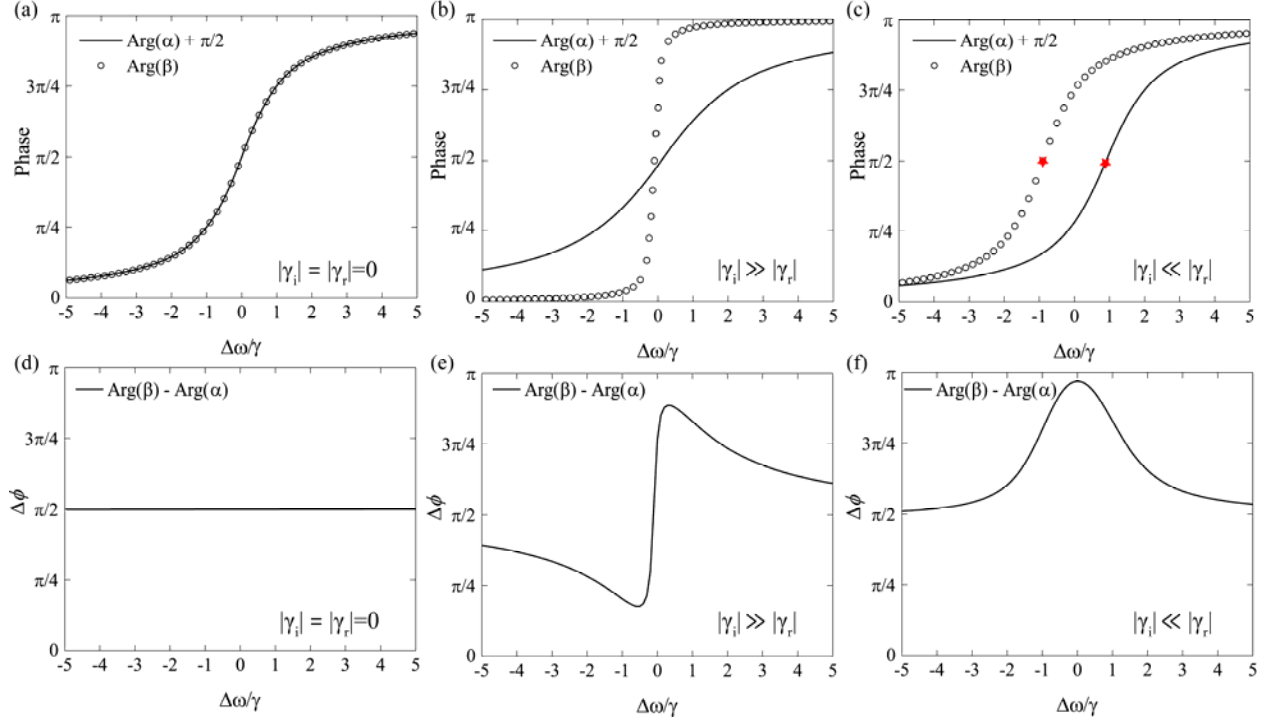


Fig. S4 Phase analysis of superradiant and subradiant Eigenstates. (a)-(c) Phases of the even and odd Eigenstates (a) without coupling, (b) when the imaginary part of coupling dominates, and (c) when the real part of coupling dominates. Note the phase of the in-phase eigenstate is always offset by $\pi/2$ for better visualization. Lines are the phase of superradiant Eigenstate while circles are for subradiant one. (d)-(f) Phase differences between the eigenstates (d) without coupling, (e) when the imaginary part of coupling is dominated, and (f) when the real part of coupling is dominated. Without coupling, the phase difference is always $\pi/2$. In great contrast, the couplings deviate the phase difference from $\pi/2$ by either changing the bandwidth (e) or shifting Eigen-frequency (f).

Next, we look at the impact of the real part of the coupling by choosing a case with $|\gamma_r| \gg |\gamma_i|$. The real part of the coupling lifts the energy degeneracy between superradiant and subradiant Eigenstates. The Eigen-frequency of the superradiant eigenstate becomes $\omega_0 + \gamma_r$, whereas that of the subradiant Eigenstate becomes $\omega_0 - \gamma_r$. These Eigen-frequencies are the centers of the phase swing as shown by the stars in Fig. S4c. The lifting of the degeneracy splits the two phase evolution curves and this also results in a spectral regime where the phase difference deviates significantly from $\pi/2$ (Fig. S4f). However, the real part of the coupling cannot be much stronger than the bandwidth of the resonators, in which case the two Eigenstates energies are split so far that interference effects become weak.

Section 2-c. Coupled mode theory: Calculation of the real and the imaginary parts of coupling coefficients

In this section, we show the calculation of the real and the imaginary parts of coupling coefficients between two coupled resonant modes in detail.

The imaginary part of coupling coefficient: The imaginary part of coupling measures the indirect interaction between the resonant modes, where photons radiated by one of the resonant modes coupled back to the other resonant modes through the continuum. This is often referred as real-photon interaction in quantum electrodynamics [14-15]. In the absence of excitation light and absorption loss, the coupled mode equation for two coupled resonant modes is:

$$i \frac{d}{dt} \begin{pmatrix} a_1 \\ a_2 \end{pmatrix} = \begin{pmatrix} \omega_0 - i\gamma & 0 \\ 0 & \omega_0 - i\gamma \end{pmatrix} \begin{pmatrix} a_1 \\ a_2 \end{pmatrix} + \begin{pmatrix} 0 & \gamma_r + i\gamma_i \\ \gamma_r + i\gamma_i & 0 \end{pmatrix} \begin{pmatrix} a_1 \\ a_2 \end{pmatrix} \quad (S12)$$

Here a_1 and a_2 are the resonant amplitudes. $|a_{1,2}|^2$ is normalized to represent the energy of the resonant modes. γ is the radiative decay rate of the resonant modes. The amplitudes of a resonant mode decays into the continuum due to coupling to outgoing plane waves. The radiating field can be described by the superposition of many plane waves. The amplitude of the plane wave propagating in the θ direction is given by:

$$S_{rad}(\theta) = \kappa_\theta \begin{pmatrix} e^{i\frac{\pi \sin(\theta)d}{\lambda}} & e^{-i\frac{\pi \sin(\theta)d}{\lambda}} \end{pmatrix} \begin{pmatrix} a_1 \\ a_2 \end{pmatrix} \quad (S13)$$

where κ_θ is the coupling rate of the resonant amplitude due to radiation to the continuum and $|S_{rad}|^2$ is the power. Each different multipolar mode will feature a different angular dependence for κ_θ . The units for κ_θ and $|S_{rad}|^2$ are 1/sec and W, respectively. The total power radiated by the coupled resonator system can be calculated by integrating the power radiated by all the plane waves as:

$$\begin{aligned} P_{rad} &= \int_{-\pi}^{\pi} d\theta S_{rad}^*(\theta) S_{rad}(\theta) \\ &= \begin{pmatrix} a_1^* & a_2^* \end{pmatrix} \begin{pmatrix} \int_{-\pi}^{\pi} d\theta \kappa_\theta^* \kappa_\theta & \int_{-\pi}^{\pi} d\theta \kappa_\theta^* \kappa_\theta e^{-i\frac{2\pi \sin(\theta)d}{\lambda}} \\ \int_{-\pi}^{\pi} d\theta \kappa_\theta^* \kappa_\theta e^{i\frac{2\pi \sin(\theta)d}{\lambda}} & \int_{-\pi}^{\pi} d\theta \kappa_\theta^* \kappa_\theta \end{pmatrix} \begin{pmatrix} a_1 \\ a_2 \end{pmatrix} \\ &= \begin{pmatrix} a_1^* & a_2^* \end{pmatrix} \begin{pmatrix} \int_{-\pi}^{\pi} d\theta \kappa_\theta^* \kappa_\theta & \int_{-\pi}^{\pi} d\theta \kappa_\theta^* \kappa_\theta \cos\left(\frac{2\pi \sin(\theta)d}{\lambda}\right) \\ \int_{-\pi}^{\pi} d\theta \kappa_\theta^* \kappa_\theta \cos\left(\frac{2\pi \sin(\theta)d}{\lambda}\right) & \int_{-\pi}^{\pi} d\theta \kappa_\theta^* \kappa_\theta \end{pmatrix} \begin{pmatrix} a_1 \\ a_2 \end{pmatrix} \quad (S14) \end{aligned}$$

The diagonal term $\int_{-\pi}^{\pi} d\theta \kappa_{\theta}^* \kappa_{\theta}$ indicates the radiative decay rate γ of the resonant mode. The off-diagonal term $\int_{-\pi}^{\pi} d\theta \kappa_{\theta}^* \kappa_{\theta} \cos\left(\frac{2\pi \sin(\theta)d}{\lambda}\right)$ quantifies the degree of overlap between the far-field radiation patterns from the two neighboring resonators.

On the other hand, the total radiation energy can also be calculated by examining the decay of energy in the resonators:

$$\begin{aligned}
P_{rad} &= -\frac{d}{dt} \left((a_1^* \ a_2^*) \begin{pmatrix} a_1 \\ a_2 \end{pmatrix} \right) = -\left(\frac{d}{dt} (a_1^* \ a_2^*) \right) \begin{pmatrix} a_1 \\ a_2 \end{pmatrix} - (a_1^* \ a_2^*) \frac{d}{dt} \begin{pmatrix} a_1 \\ a_2 \end{pmatrix} \\
&= -i(a_1^* \ a_2^*) \begin{pmatrix} \omega_0 + i\gamma^* & \gamma_r - i\gamma_i^* \\ \gamma_r - i\gamma_i^* & \omega_0 + i\gamma^* \end{pmatrix} \begin{pmatrix} a_1 \\ a_2 \end{pmatrix} + i(a_1^* \ a_2^*) \begin{pmatrix} \omega_0 - i\gamma & \gamma_r + i\gamma_i \\ \gamma_r + i\gamma_i & \omega_0 - i\gamma \end{pmatrix} \begin{pmatrix} a_1 \\ a_2 \end{pmatrix} \\
&= (a_1^* \ a_2^*) \begin{pmatrix} \gamma + \gamma^* & -\gamma_i - \gamma_i^* \\ -\gamma_i - \gamma_i^* & \gamma + \gamma^* \end{pmatrix} \begin{pmatrix} a_1 \\ a_2 \end{pmatrix} \\
&= (a_1^* \ a_2^*) \begin{pmatrix} 2\gamma & -2\gamma_i \\ -2\gamma_i & 2\gamma \end{pmatrix} \begin{pmatrix} a_1 \\ a_2 \end{pmatrix}
\end{aligned} \tag{S15}$$

By comparing Eq. S15 and Eq. S14, it's straightforward to obtain:

$$\gamma = \frac{1}{2} \int_{-\pi}^{\pi} d\theta \kappa_{\theta}^* \kappa_{\theta} \tag{S16a}$$

$$\gamma_i = -\frac{1}{2} \int_{-\pi}^{\pi} d\theta \kappa_{\theta}^* \kappa_{\theta} \cos\left(\frac{2\pi \sin(\theta)d}{\lambda}\right) \tag{S16b}$$

In order to calculate the imaginary part of coupling coefficients, it's necessary to obtain the far-field radiation pattern and the radiative decay rate γ of the resonant modes. As an example, we consider a pair of parallel nanowires as in the main text. The cross-sectional dimensions of the nanowires are 100 nm by 100 nm and the gap between them is also 100 nm. To make the discussion more concise, the refractive indices of the nanowires are fixed at $4 + j0.025$ and we assume they are embedded in free space. Each nanowire supports two degenerate TM modes at the same wavelength of 610 nm, i.e. the $|A_x\rangle$ and $|A_y\rangle$ modes. As shown in Fig. S5a, the $|A_x\rangle$ mode is a magnetic dipole along the x axis, which can be clearly seen by its field profile (top panel). Its far-field radiation pattern has a $\cos^2\theta$ shape (bottom panel). The radiative decay rate γ is obtained by measuring the full width at half maximum (FWHM) of the absorption spectrum. We excited the $|A_x\rangle$ mode by putting line current sources in a single nanowire and calculating the spectrum of the absorbed power from FDFD simulation. The line current sources are carefully distributed according to the mode profile. The radiative decay rate γ then is obtained as $\gamma = \frac{1}{2}FWHM - \gamma_a$, where the absorption rate γ_a can be calculated by integrating $\sigma(\omega)|E|^2$ in the structures where $\sigma(\omega)$ is the conductivity at the angular frequency ω and E is the electric field.

The decay rate $\kappa_{\theta x}$ for the $|A_x\rangle$ mode then is given by $\kappa_{\theta x} = \sqrt{\frac{2\gamma}{\pi}} \cos\theta$. The imaginary part of coupling coefficient for the $|A_x\rangle$ mode in our structures then can be calculated as:

$$\begin{aligned}
\gamma_{ix} &= -\frac{1}{2} \int_{-\pi}^{\pi} d\theta \kappa_{\theta x}^* \kappa_{\theta x} \cos\left(\frac{2\pi \sin(\theta) d}{\lambda}\right) \\
&= -\frac{\gamma}{\pi} \int_{-\pi}^{\pi} d\theta \cos^2 \theta \cos\left(\frac{2\pi \sin(\theta) d}{\lambda}\right)
\end{aligned} \tag{S17}$$

On the other hand, the $|A_y\rangle$ mode is a magnetic dipole along the y axis, which can also be clearly seen by its field profile in Fig. S5b. Its far-field radiation pattern has a $\sin^2 \theta$ shape and its decay rate $\kappa_{\theta y}$ is given by $\kappa_{\theta y} = \sqrt{\frac{2\gamma}{\pi}} \sin \theta$. Similarly, the imaginary part of coupling coefficient for the $|A_y\rangle$ mode in our structures can be calculated as:

$$\begin{aligned}
\gamma_{iy} &= -\frac{1}{2} \int_{-\pi}^{\pi} d\theta \kappa_{\theta y}^* \kappa_{\theta y} \cos\left(\frac{2\pi \sin(\theta) d}{\lambda}\right) \\
&= -\frac{\gamma}{\pi} \int_{-\pi}^{\pi} d\theta \sin^2 \theta \cos\left(\frac{2\pi \sin(\theta) d}{\lambda}\right)
\end{aligned} \tag{S18}$$

Note the imaginary part of coupling between the $|A_x\rangle$ mode and the $|A_y\rangle$ mode in different nanowires is zero, which can be directly shown as $\int_{-\pi}^{\pi} d\theta \sin \theta \cos \theta \cos\left(\frac{2\pi \sin(\theta) d}{\lambda}\right) = 0$.

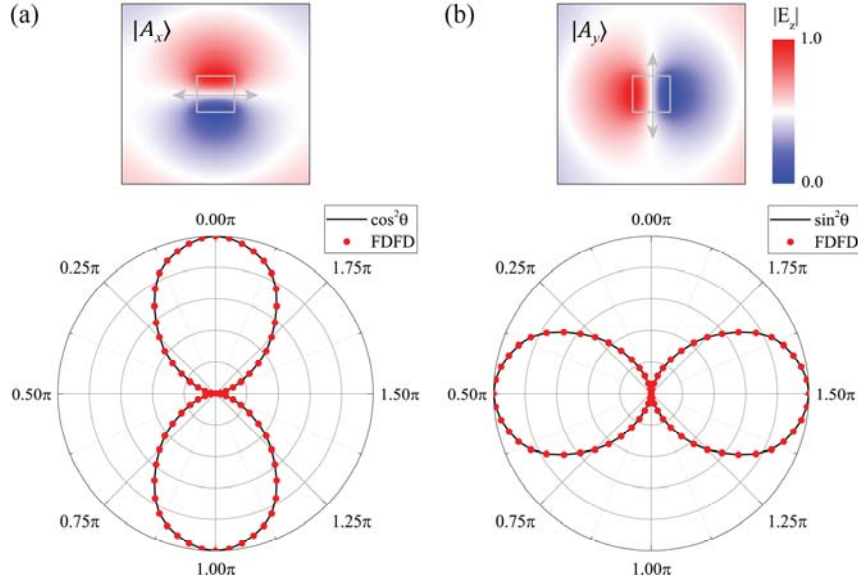


Fig. S5 Far-field radiation patterns for the $|A_x\rangle$ and $|A_y\rangle$ modes. (a) The $|A_x\rangle$ mode is a magnetic dipole in the x direction (gray arrow), whose electric field distribution is shown in the upper panel. Its far-field emission profile has a $\cos^2 \theta$ shape, which can be seen by comparing the analytic curve (black solid line) and FDFD simulation (red circles) in the lower panel. (b) The $|A_y\rangle$ mode is a magnetic dipole in the y direction (gray arrow), which has a $\sin^2 \theta$ shape far-field radiation profile.

The real part of coupling coefficient: The real part of coupling measures the direct interaction between the resonant modes, where the two resonant modes interact through virtual photons [14]. The real part of coupling coefficient between two coupled modes can be directly calculated from the overlapping of the resonant field distribution, which is given by the following equation [16]

$$\gamma_r = \frac{\omega_0}{4} \frac{\int \int dx_a dy_a \epsilon_a(x, y) \mathbf{E}_a^*(x, y) \cdot \mathbf{E}_b(x, y)}{\int_{-\infty}^{\infty} \int_{-\infty}^{\infty} dx dy |\mathbf{E}_a(x, y)|^2} \quad (\text{S19})$$

Here $\mathbf{E}_a(x, y)$ and $\mathbf{E}_b(x, y)$ are the resonant electric field from wire a and b , respectively. $\epsilon(x, y)$ is the relative dielectric function with only wire a in the space. The integral in the numerator is performed within the volume of wire a .

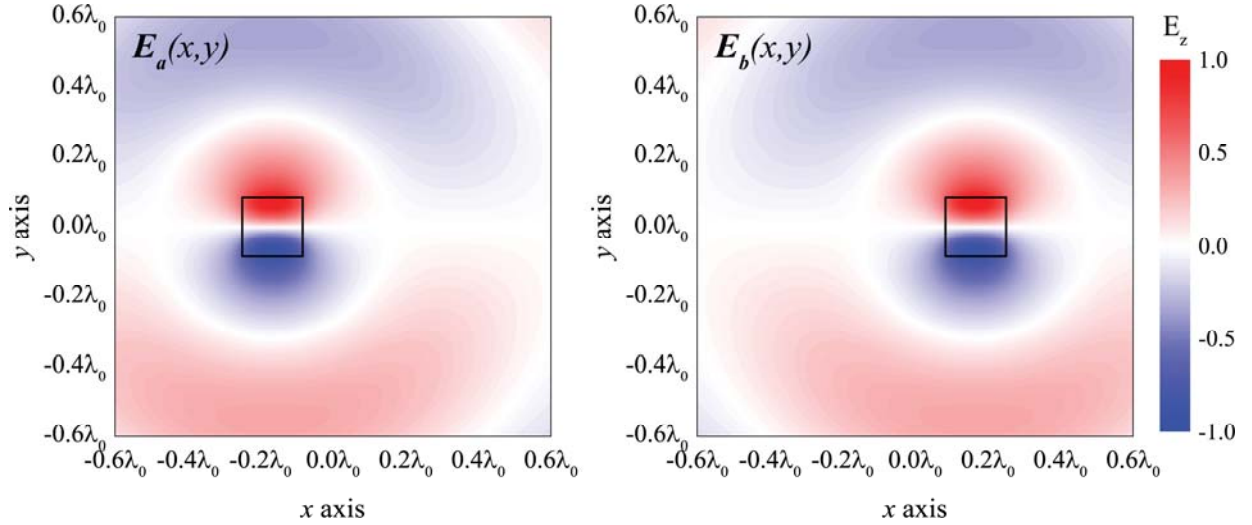


Fig. S6 Resonant electric field distributions for the modes near each wire. We plot the $|A_x\rangle$ mode as an example.

The real part of coupling coefficient can be quantified by using Finite-Difference Frequency-Domain simulations of electric fields for the relevant resonant modes. These modes are excited by putting line current sources inside the nanowires (Fig. S6), where the line current sources are carefully distributed according to the mode profile. Then we perform the integral numerically to calculate the real part of coupling coefficients.

Section 2-d. Coupled mode theory: derivation of the energy in coupled resonators in free space.

We will solve the coupled-mode equation described by Eq. S7 to obtain the energy in resonators under illumination from different incident angles. Under steady-state excitation with an angular frequency ω , Eq. S7 can be written as:

$$\begin{pmatrix} \omega - \omega_0 + i\gamma & -\gamma_r - i\gamma_i \\ -\gamma_r - i\gamma_i & \omega - \omega_0 + i\gamma \end{pmatrix} \begin{pmatrix} a_1 \\ a_2 \end{pmatrix} = i\kappa_\theta S(\theta) \begin{pmatrix} e^{-i\frac{\pi \sin(\theta)d}{\lambda}} \\ e^{i\frac{\pi \sin(\theta)d}{\lambda}} \end{pmatrix} \quad (\text{S20})$$

Therefore, we can get the resonance amplitude of the resonators as:

$$\begin{aligned}
\begin{pmatrix} a_1 \\ a_2 \end{pmatrix} &= i\kappa_\theta S(\theta) \begin{pmatrix} \omega - \omega_0 + i\gamma & -\gamma_r - i\gamma_i \\ -\gamma_r - i\gamma_i & \omega - \omega_0 + i\gamma \end{pmatrix}^{-1} \begin{pmatrix} e^{-i\varphi} \\ e^{i\varphi} \end{pmatrix} \\
&= \frac{i\kappa_\theta S(\theta)}{(\omega - \omega_0 + i\gamma)^2 + (\gamma_r + i\gamma_i)^2} \begin{pmatrix} \omega - \omega_0 + i\gamma & \gamma_r + i\gamma_i \\ \gamma_r + i\gamma_i & \omega - \omega_0 + i\gamma \end{pmatrix} \begin{pmatrix} e^{-i\varphi} \\ e^{i\varphi} \end{pmatrix} \\
&= \frac{i\kappa_\theta S(\theta)}{(\omega - \omega_0 + i\gamma)^2 + (\gamma_r + i\gamma_i)^2} \begin{pmatrix} (\omega - \omega_0 + i\gamma)e^{-i\varphi} + (\gamma_r - i\gamma_i)e^{i\varphi} \\ (\omega - \omega_0 + i\gamma)e^{i\varphi} + (\gamma_r + i\gamma_i)e^{-i\varphi} \end{pmatrix} \quad (S21)
\end{aligned}$$

Here we define $\varphi = \frac{\pi \sin(\theta)d}{\lambda}$ for simplification. The ratio between the resonator's energies then is:

$$\left| \frac{a_2}{a_1} \right|^2 = \frac{(\omega - \omega_0 + \gamma_i \sin 2\varphi + \gamma_r \cos 2\varphi)^2 + (\gamma + \gamma_i \cos 2\varphi - \gamma_r \sin 2\varphi)^2}{(\omega - \omega_0 - \gamma_i \sin 2\varphi + \gamma_r \cos 2\varphi)^2 + (\gamma + \gamma_i \cos 2\varphi + \gamma_r \sin 2\varphi)^2} \quad (S22)$$

It's straightforward to see that the ratio is always 1 if there is no coupling between the resonators, *i.e.* $\gamma_i = 0$ and $\gamma_r = 0$.

Section 2-e. Coupled mode theory for acoustic resonators

In this section, we show that coupled acoustic resonators also follow the same coupled mode theory. We follow the notation used in Ref [17]. Considering two identical acoustic resonators that are coupled to N scattering channels, the effective Hamiltonian is given by

$$\mathbf{H}_{eff} = \begin{pmatrix} E_0 & 0 \\ 0 & E_0 \end{pmatrix} - i\pi \sum_{n=1}^N \begin{pmatrix} V_n \\ V_n \end{pmatrix} \begin{pmatrix} V_n^* & V_n^* \end{pmatrix} \quad (S23)$$

where E_0 is the eigenenergy of the resonator. $V_{1,n}$ and $V_{2,n}$ are the coupling coefficients of the 1st and 2nd resonator to the n th scattering channel, respectively.

The general solution to the effective Hamiltonian can be written as:

$$\psi = \chi_1 \phi_1 + \chi_2 \phi_2 + \sum_{n=1}^N f_n \quad (S24)$$

Here ϕ_1 and ϕ_2 are the eigenfunctions in the 1st and 2nd resonators, respectively. χ_1 and χ_2 are resonance amplitudes, respectively. The general solution of waves in each scattering channel is written as a superposition of incoming and outgoing waves [17]:

$$f_n = p_n u_n(\xi) e^{ik_n \xi} + q_n u_n(\xi) e^{-ik_n \xi} \quad (S25)$$

where p_n and q_n are the amplitudes of the incoming and outgoing waves, respectively. $u_n(\xi)$ is the eigen wavefunction in the n th scattering channel.

In order to find the resonance amplitudes χ_1 and χ_2 , we can evaluate the scalar products $\langle \phi_m | \mathbf{H}_{eff} - E | \psi \rangle = 0$, where $m = 1, 2$. The scalar products lead us to a simple coupled mode equation for the resonance amplitudes χ_1 and χ_2 . For the general case of two coupled acoustic resonators, it can be written in the matrix form as:

$$\begin{pmatrix} E_0 - E - i\pi g & 0 \\ 0 & E_0 - E - i\pi g \end{pmatrix} \begin{pmatrix} \chi_1 \\ \chi_2 \end{pmatrix} - i\pi \begin{pmatrix} 0 & g_c \\ g_c & 0 \end{pmatrix} \begin{pmatrix} \chi_1 \\ \chi_2 \end{pmatrix} = -i2\pi \begin{pmatrix} V_{inc} p_{inc} e^{i\varphi_1} \\ V_{inc} p_{inc} e^{i\varphi_2} \end{pmatrix} \quad (S26)$$

where $g = \sum_{n=1}^N V_n V_n^*$ describes the total decay rate of the resonance to the scattering channels, and $g_c = \sum_{n=1}^N V_n V_n^* e^{i(\varphi_1 - \varphi_2)}$ describes the indirect interaction between the resonators through the scattering channels. φ_1 and φ_2 are the incident phase at the 1st and 2nd resonators, respectively. The interaction between coupled acoustic resonators is governed by a non-Hermitian Hamiltonian. This above equation shows that the wave coupling dynamics is the same for acoustic resonators and for optical waves (Eq. S7).

Section 3. Resonance is crucial to angle detection in a subwavelength space.

Resonance plays a critical role in determining the performance of an angle-sensing photodetector. Here, we show that the performance decreases as the resonance diminishes. We replace Si nanowires with a material having low refractive index, for example, $n = 1.5 + i0.1$. The same structure is used as in Fig. 2c, the resonant frequency is shifted away since visible light cannot be sufficiently confined in such nanowires due to its low index value. Under this circumstance, the absorption cross section ratio between two nanowires is extremely low for both polarizations over entire range of incident angles (Fig. S7). The resonator is critical as it can effectively create a shadow larger than its own geometric size, i.e. significantly reduced the absorption cross section of an adjacent resonator. A large shadow makes it easier to create a large contrast between two nanowires.

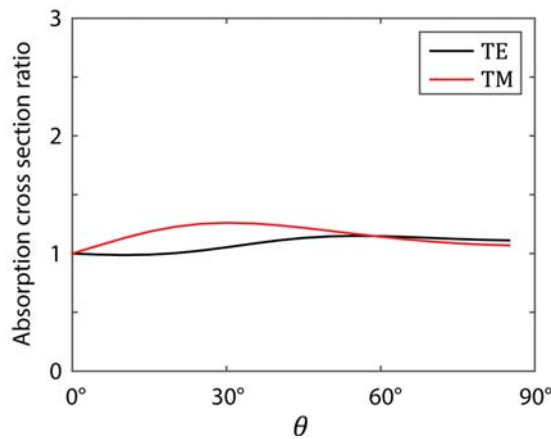


Fig. S7 Absorption cross section ratio of angle-sensing photodetector having two nanowires with complex refractive index $n = 1.5 + i0.1$. Physical structure is the same as in Fig. 2c with $d=100$ nm.

Section 4. Effect of spacing d and optical absorption γ_a

The coupling strength generally is determined by the geometry and material of the resonators and the spacing d between them. In this section, we discuss how the contrast ratio is affected by the spacing and the material loss. In general, both the imaginary and the real part of coupling increase as the spacing d decreases. Figure S8a shows the relation between the imaginary part of coupling and the spacing d for resonators with isotropic radiation patterns, i.e. coupling rate κ_θ being the same for all incident angles. As the spacing decreases, the coupling generally gets stronger. At the same time, the contrast ratio for the stored energy in the resonators is increased. Figure S8b show a polar plot of the contrast ratio for different spacing. As the spacing decreases, the overall angular response gets stronger, i.e. larger energy storage ratios are achieved. Typically, when two resonators are $0.01 \lambda_0$ away, their energy ratio can exceed 30 dB. The dashed lines on the left-hand side indicate negative dB values. In these plots, we did not consider the effect of the real part of couplings, which could enhance or suppress the maximum ration depending on specific configuration. The detailed calculation can be always done by Eq. S22 given specific near-field distribution of the resonator.

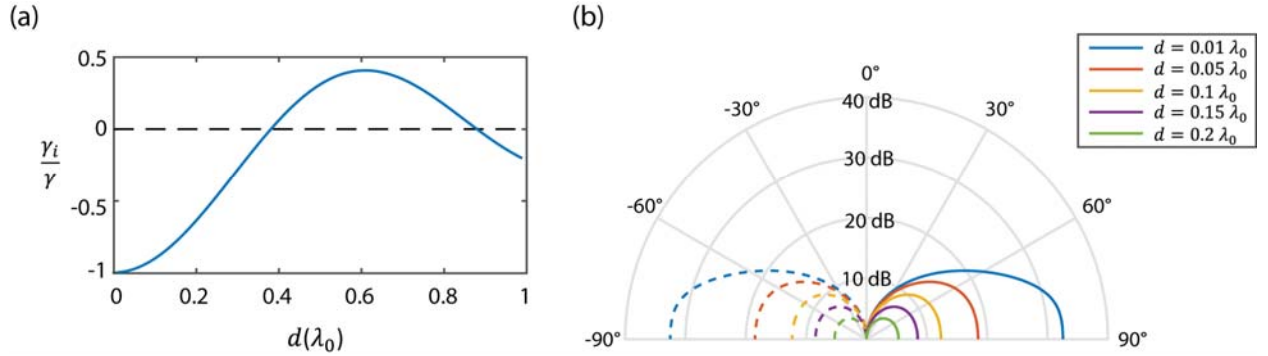


Fig. S8 Effect of spacing d between two resonators. (a) The relation between the imaginary part of coupling and the spacing. (b) Polar plot of energy ratio vs incident angle for different distances between two optical resonators. As the distance between two resonators get smaller, higher energy ratio is achieved. Energy ratio of dashed lines on the left-hand side indicate negative dB values. $\gamma = 0.01\omega_0$ and $\gamma_a = 0$ are used for calculation.

The material loss is characterized by a dissipation rate γ_a , which can be straightforwardly included in the total decay rate γ in Eq. S7. In general, it will reduce the maximum contrast ratio as the quality factor of the resonator decreases. Figure S9 shows the decrease in the maximum contrast ratio as the optical absorption increases.

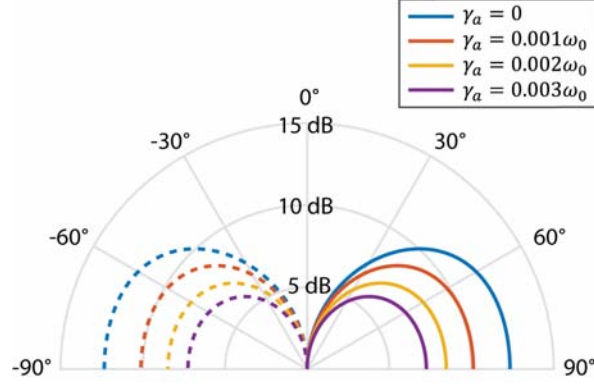


Fig. S9 Polar plot of energy ratio vs incident angle for various optical absorption. $d = 0.1 \lambda_0$ and $\gamma = 0.01\omega_0$ is used for the calculation. Energy ratio of dashed lines on the left hand side indicate negative dB values.

Section 5. Modal profiles and spectral response of resonant Si nanowires

Figure S10 shows the absorption cross section spectrum and field profiles of a single nanowire with a 100 nm width and height on top of a SiO₂ substrate for normal incident light. The finite difference frequency domain (FDFD) method was used for the calculations. Figure S10a shows the spectrum for TE polarized light and the field profiles of $|H_z|^2$ at each of the resonance peaks are shown. The lowest resonant mode for TE polarized light appears around a 590 nm wavelength and higher order modes are seen around 450 nm and 390 nm. Figure S10b shows the spectrum for TM polarized light and the field profiles of $|E_z|^2$ at each of the resonance peaks are shown. The fundamental mode for TM polarized light is located beyond 1 μm wavelength and is not shown. Higher-order modes are seen around wavelengths of 600 nm, 440 nm, and 400 nm.

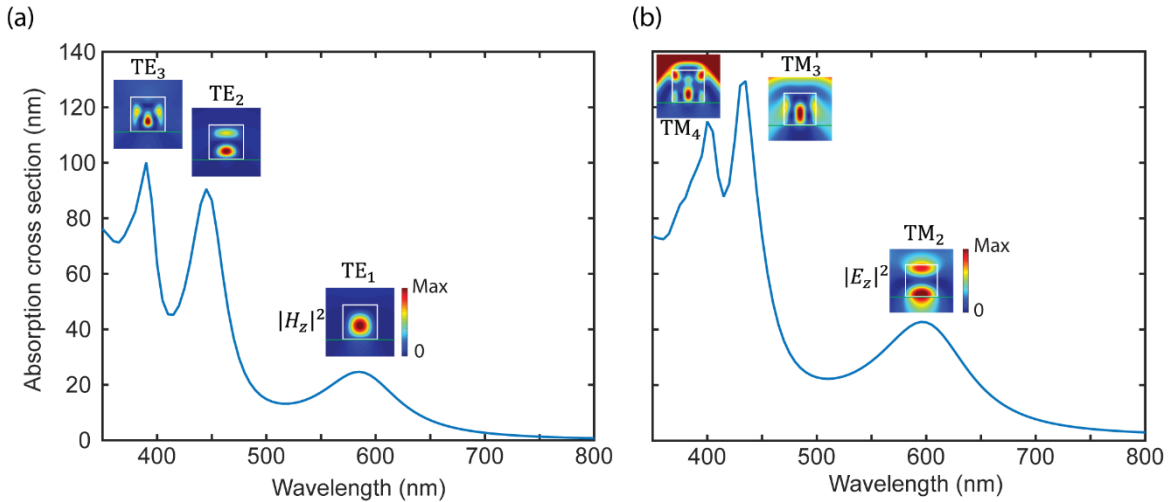


Fig. S10 Absorption cross section spectrum. (a) Absorption cross section spectrum and its $|H_z|^2$ field profiles on resonance peaks for a Si nanowire on top of a SiO₂ substrate with TE polarization. Width and height of Si nanowire are 100 nm. (b) Absorption cross section spectrum and its $|E_z|^2$ field profile of Si nanowire for TM polarization.

Section 6. Coupled mode theory for nanowires with two degenerate modes

Our nanowire supports both the fundamental TE mode and the second-order TM mode around 600 nm wavelength. The TE mode is singly degenerate mode and the coupling coefficients are always the same for all the incident angles. However, the TM mode is doubly degenerate and two distinct modes can be identified for which light oscillates in either the horizontal or vertical direction. This degeneracy results in a resonant electric field distribution that is incident-angle dependent. As a result, the real part of coupling between two closely-spaced nanowires also appears to be incident-angle dependent. Obviously, this case requires careful consideration. Here, we discuss how the apparent angle dependence can be removed by using all degenerate modes in the coupled mode theory.

Figure S11 shows the electric field distributions around a pair of nanowires in which the doubly degenerate second-order TM mode is excited by a plane wave incident from different directions. The dimensions and the spacing between of the nanowire are the same as in our experiments, but the substrate is removed for educational purposes. The incident wavelength is 550 nm, which is also the same with our experiment. The index of the nanowires at this wavelength is $4 + j0.025$. For different incident angles, different magnetic dipole moments (gray arrows) are induced. The near-field distribution is different when comparing Fig. S11a and S11b. As a result, the real part of coupling as calculated from the field overlap would be different as well. Next, we will show how one could use all four modes in this system to remove the apparent dependence of the real part of coupling on the incident angle.

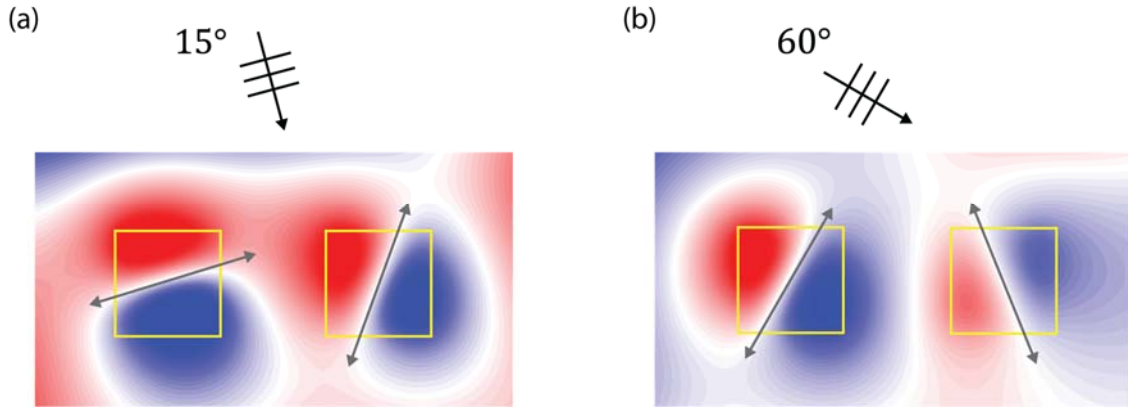


Fig. S11 Electric field distribution of doubly degenerate second-order TM mode. (a)-(b) Electric field profile for TM mode with 15°(a) and 60°(b) incident angle. Grey arrow represents the direction of the magnetic dipole. The dimensions of the nanowire are 100 nm by 100 nm and the gap between the nanowires is 100 nm, which are the same with the nanowires in our experiment except without the substrate. The incident wavelength is 550 nm, which is also the same with our experiment.

Each nanowire supports two degenerate modes $|A_x\rangle$ and $|A_y\rangle$, which are shown in Fig. S12a. Under the illumination of a particular incident angle, the excited mode can always be written as the linear combination of two modes $|a\rangle = a_x|A_x\rangle + a_y|A_y\rangle$ as shown in Fig. S12b.

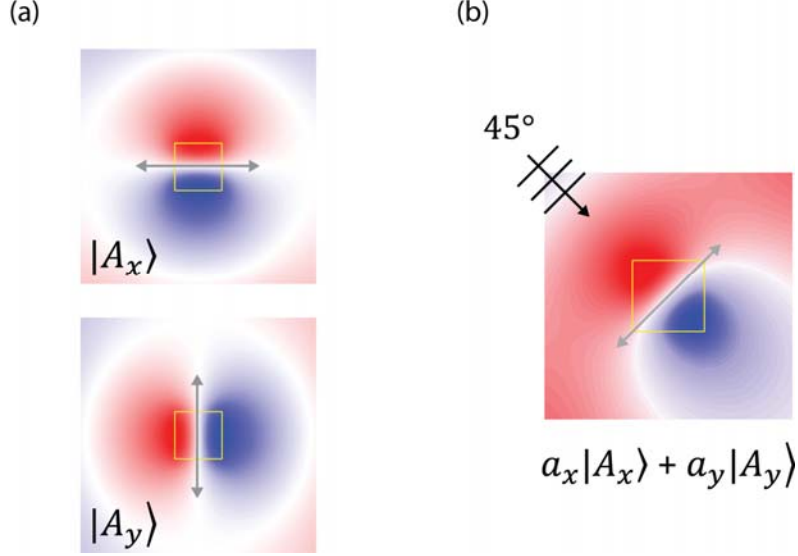


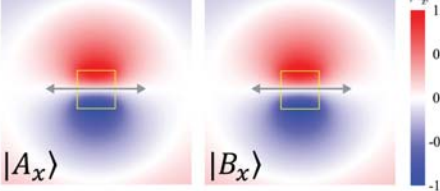
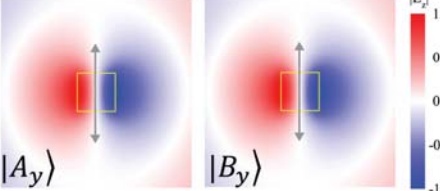
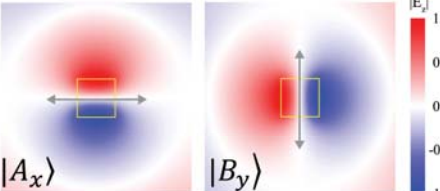
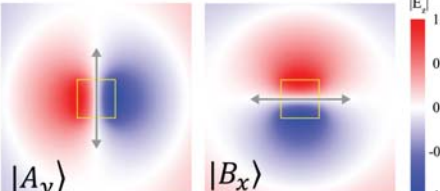
Fig. S12 Mode profiles of degenerate mode. (a) Mode profiles for two degenerate states in TM mode. (b) With incident light from 45° angle, a linear combination of the states in (a) is excited

When we consider the case shown in the coupled nanowires in Fig. S11, we need to consider all 4 modes, i.e. $|A_x\rangle$, $|A_y\rangle$ for the left nanowire, and $|B_x\rangle$, $|B_y\rangle$ for the right nanowires. The coupled mode equation for these modes is given by:

$$\frac{d}{dt} \begin{pmatrix} a_x \\ b_x \\ a_y \\ b_y \end{pmatrix} = \begin{pmatrix} \omega_0 - i\gamma & \gamma_{rx} + i\gamma_{ix} & 0 & 0 \\ \gamma_{rx} + i\gamma_{ix} & \omega_0 - i\gamma & 0 & 0 \\ 0 & 0 & \omega_0 - i\gamma & \gamma_{ry} + i\gamma_{iy} \\ 0 & 0 & \gamma_{ry} + i\gamma_{iy} & \omega_0 - i\gamma \end{pmatrix} \begin{pmatrix} a_x \\ b_x \\ a_y \\ b_y \end{pmatrix} + iS(\theta) \begin{pmatrix} \kappa_{\theta x} \cos(\theta) e^{-i\frac{\pi \sin(\theta)d}{\lambda}} \\ \kappa_{\theta x} \sin(\theta) e^{i\frac{\pi \sin(\theta)d}{\lambda}} \\ \kappa_{\theta y} \cos(\theta) e^{-i\frac{\pi \sin(\theta)d}{\lambda}} \\ \kappa_{\theta y} \sin(\theta) e^{i\frac{\pi \sin(\theta)d}{\lambda}} \end{pmatrix} \quad (\text{S27})$$

Here $\kappa_{\theta x}$ and $\kappa_{\theta y}$ are the coupling coefficients to the incident waves with an incident angle θ . The amplitudes of $|A_x\rangle$, $|A_y\rangle$, $|B_x\rangle$ and $|B_y\rangle$ modes in the nanowires are given by a_x , a_y , b_x and b_y , respectively. The real part of coupling coefficients $\gamma_{rx/ry}$ and the imaginary part of coupling coefficients $\gamma_{ix/iy}$ are calculated and listed in Table. S1. The coupling between the $|A_y\rangle$ and $|B_y\rangle$ and that between $|A_x\rangle$ and $|B_y\rangle$ modes is extremely low and negligible. For ideal dipoles, because of the symmetry, it will be exactly zero despite the spatial displacement [18].

Table S1. Coupling coefficients for different modes.

	$\gamma_{rx} = -0.005\omega_0$ $\gamma_{ix} = 0.0176\omega_0$
	$\gamma_{ry} = 0.041\omega_0$ $\gamma_{iy} = 0.0688\omega_0$
	$\gamma_r \sim 0$ $\gamma_i = 0$
	$\gamma_r \sim 0$ $\gamma_i = 0$

In this 4-mode model, the real part of coupling coefficients are angle-independent. Their values are calculated and shown in Table 1. We can then solve the coupled mode equation with these fixed coupling coefficients, and calculate the absorption ratio for the two nanowires $\frac{|a_x|^2 + |a_y|^2}{|b_x|^2 + |b_y|^2}$ for different incident angles. The results are plotted in Fig. S13 as black solid line. Compared to numerical simulation results (red circles), which are obtained by solving the Maxwell's equations using finite-difference method in the frequency domain (FDFD), the analytic results agree with FDFD simulation very well. The imaginary part of coupling strength between the $|A_y\rangle$ and $|B_y\rangle$ modes is increased as compared to our experiment. As a result, the absorption ratio is increased. The mismatch between CMT and FDFD method in Fig. S13 is due to the fact that CMT is built upon the assumption of ideal dipoles while the FDFD method considers the actual dimensions of nanowires.

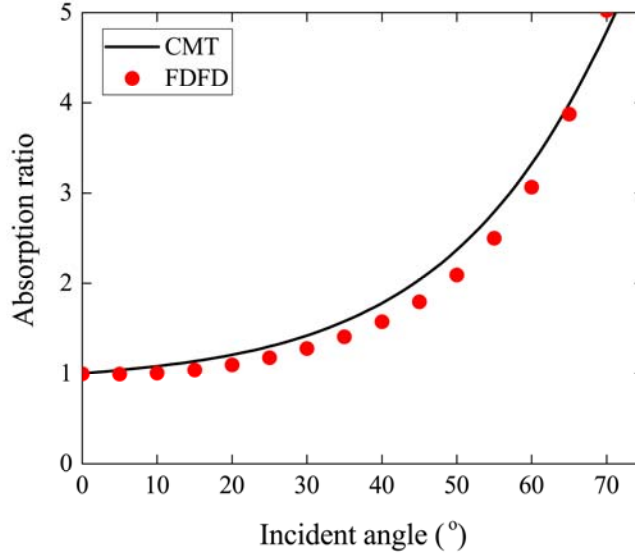


Fig. S13 Absorption ratio as a function of incident angle.

Section 7. Phased array and direction finding in the radio frequency regime

Angle-sensing has a wide range of applications in the radio frequency (RF) regime, including most prominently for direction finding. This includes a recent work on employing subwavelength antennas [19]. RF direction finding is relatively straightforward because the phase information of RF signals are easily preserved in the detection process. As a result, most RF methods rely on coherently combining multiple signals received at different locations or rely on antennas that are much larger than the operating wavelength.

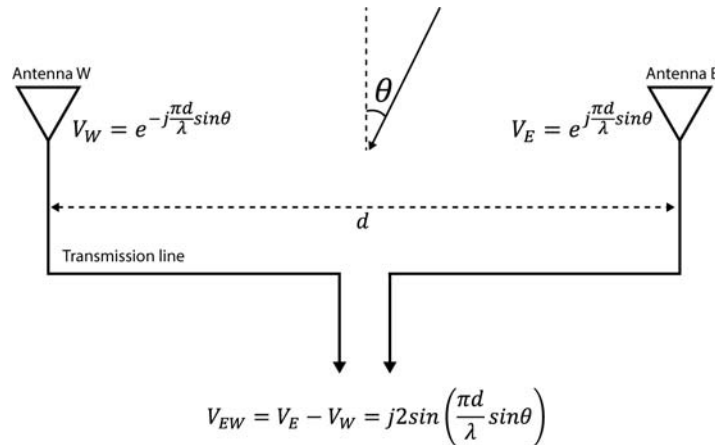


Fig. S14 Schematic of a direction finding system using two antennas. Two antennas are connected through a transmission line. Voltage induced at the two antennas by an incident wave are compared at the output of the transmission line.

Here we briefly discuss the mechanism of direction finding developed in the microwave regime. As an example, direction finding can be implemented using an Adcock antenna [20-21]. Figure

S14 shows a pair of antennas that are used in an Adcock antenna. When two antennas are spaced by a distance d , there will be a phase difference between the signals that the two antennas receive. Assuming the center of the two antennas as the reference point, the voltage induced at Antenna E and Antenna W by an incident wave having an incident angle θ can be expressed as $V_E = e^{j\frac{\pi d}{\lambda}\sin\theta}$ and $V_W = e^{-j\frac{\pi d}{\lambda}\sin\theta}$, respectively. Comparing these two coherent signals, we can get the difference:

$$V_{EW} = V_E - V_W = j2\sin\left(\frac{\pi d}{\lambda}\sin\theta\right) \quad (\text{S28})$$

These methods rely on coherent manipulation of the signals received by antennas, which is not readily available in the optical regime.

Phased array functions very well even without coupling. They operate by leveraging far-field interference. Most phased arrays are much larger than wavelength size, and the mutual coupling between elements is a perturbation that one need to be aware of when designing a system with optimal directionality. In contrast, the mutual (anti-Hermitian) coupling is the enabling mechanism in our angle detectors. Without the coupling, the proposed angle detector will fail completely. One noteworthy effect of coupling-enable angle resolution is that its performance actually increases as the inter-resonator distance d decreases, as shown in Fig. S8b. In contrast, phased arrays, which primarily relying on far-field interference, exhibit degraded angle directivity as sizes decrease which can be seen from Eq. S28. It shares the same drawbacks as the ears used by large animals: the interaural difference diminishes when the head size decreases far below the wavelength.

Section 8. Simulation of short nanowires for angle sensing.

The length of the nanowires shown in Fig. 4b is $10\ \mu\text{m}$, which is used to avoid light scattering from the large electrodes. The length of the nanowires can be reduced down to a subwavelength length and yet an angle –sensing pixel can maintain its angular response. We show the angular response for nanowires that are only 300 nm long. Figure S15a shows the schematic of two parallel Si nanowires that are 300 nm long and placed on top of a SiO_2 substrate. The gap between the two nanowires are 100 nm and the nanowires feature a $100\ \text{nm} \times 100\ \text{nm}$ cross-sectional area. The angular response of these angle sensing pixel is shown in Fig. S15b. The energy ratio between the two nanowires is 1 at normal incidence ($\theta = 0^\circ$) and maintains a monotonically increasing angular response up to $\theta = 40^\circ$ under illumination with unpolarized light.

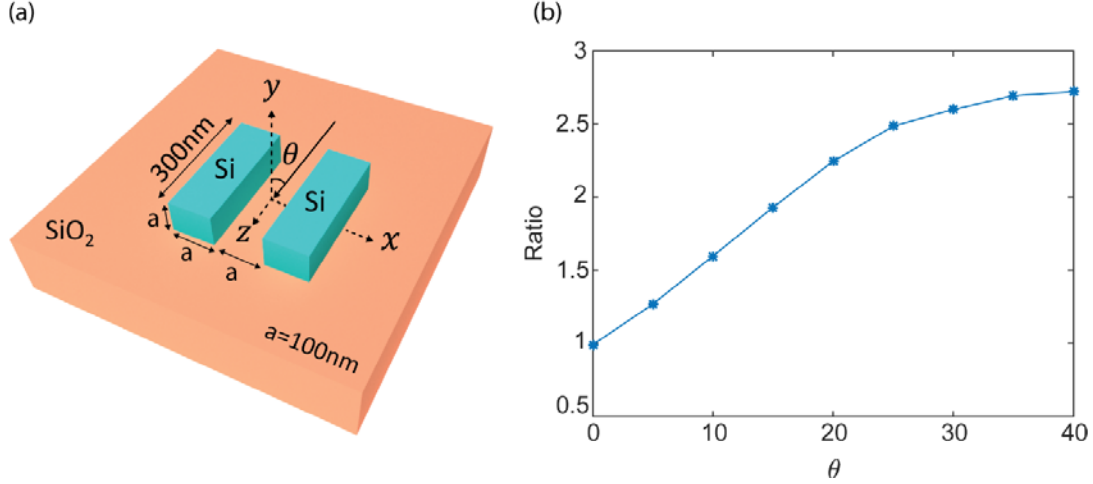


Fig. S15 Schematic of short Si nanowires and its energy ratio. (a) Two parallel Si nanowires are placed on top of SiO₂ substrate. Length of the nanowires are 300 nm. The width and the height are 100 nm and the distance between the two nanowires is 100 nm, i.e. $a=100 \text{ nm}$. (b) The energy ratio vs incident angle for two nanowires shown in (a). Illumination with unpolarized light is assumed for the calculations.

Section 9. Experimental Voltage-current relation and Responsivity

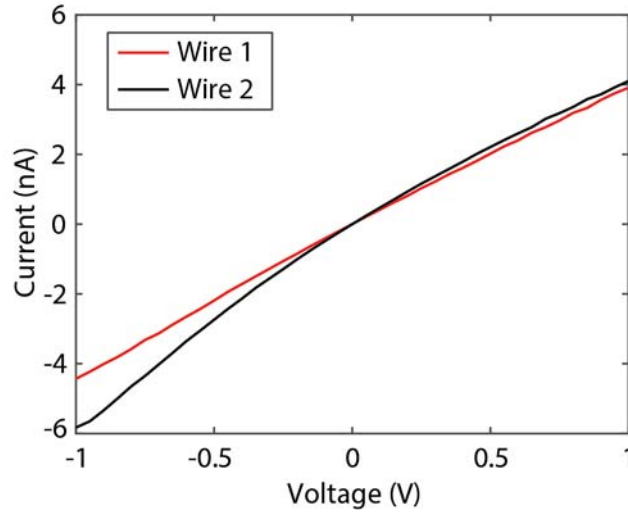


Fig. S16 Voltage-current measurement of two Si nanowires. Both nanowires show a resistor-like behavior.

Figure. S16 shows the voltage-current relationship of both nanowires without incident light i.e. dark current. A DC power supply is used to apply the voltage and measure the current. Both nanowires show an Ohmic contact. As a result, the photodetection device is a photoconductor-type detector.

The responsivity of two nanowires at 550 nm wavelength are 0.52 A/W and 0.34 A/W for TE mode and 0.5 A/W and 0.31 A/W for TM mode. It is calculated by considering the geometrical area of the nanowire and the incident power density, which is estimated to be around 60 W/m².

We note that nanowires increase the absorption cross sections, which often exceed the geometric cross sections. Near-unity absorption can be realized in nanowire arrays in Ref [22].

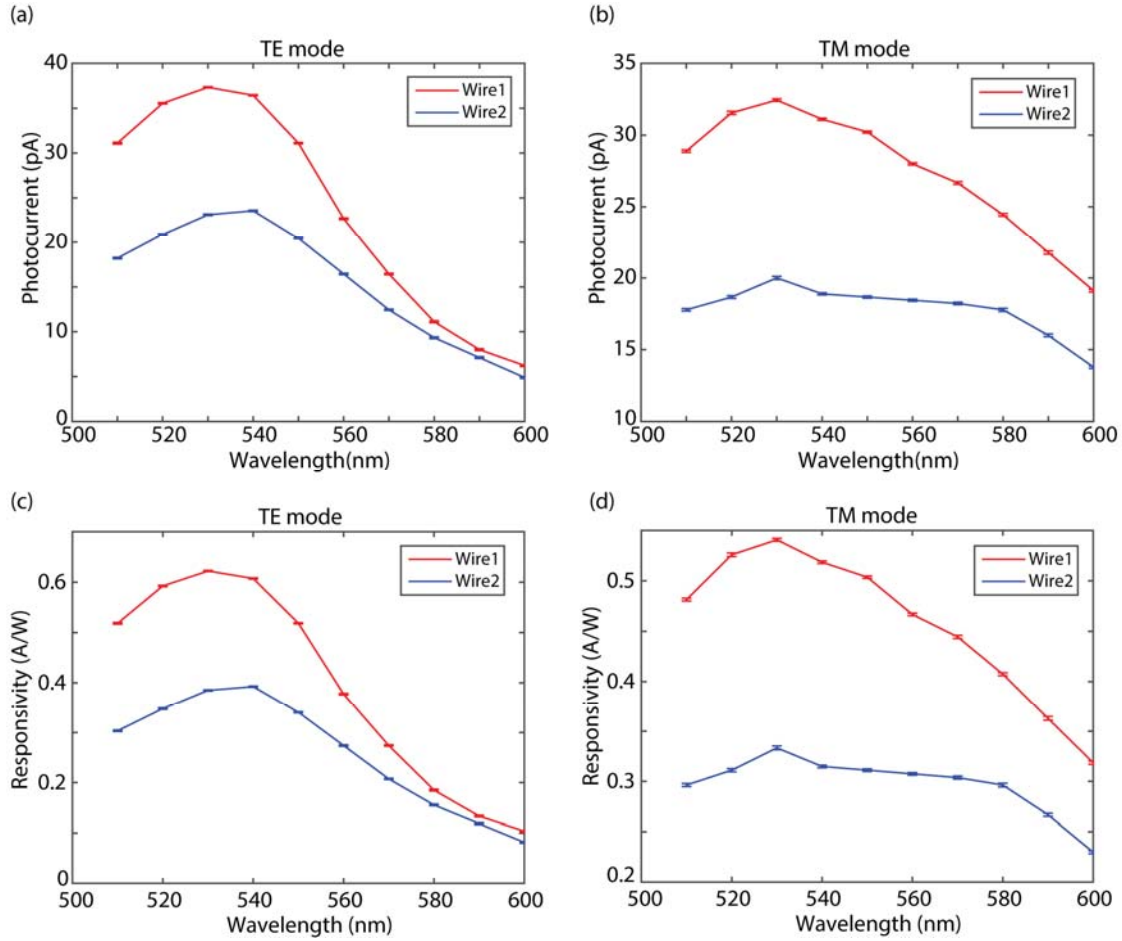


Fig. S17 The spectra of the measured photocurrent and calculated responsivity of two nanowires under illumination of TE and TM light.

The two nanowires have different responsivity. They differ by a factor of 1.53, which could be attributed to fabrication variation. This responsivity difference is factored in when we calculate the ratio of the two photocurrents in the manuscript.

Section 10. Different size nanowires for angle sensing.

The difference in photocurrent responsivity does not affect the angle sensing capability because the photocurrent of each nanowire is normalized by its own maximum photocurrent. The fabrication variation could lead to a small change in the observed resonant frequencies. But this does not significantly affect the angle sensing capability because the resonance has a broader bandwidth than the variation of the resonant frequency. Figure S18 shows energy ratio vs incident angle (θ) when the nanowire size is detuned by $\pm 5\%$ and for TM illumination. It can be seen that even when the two nanowires have different sizes, the ratio can still be used to resolve the incident angle.

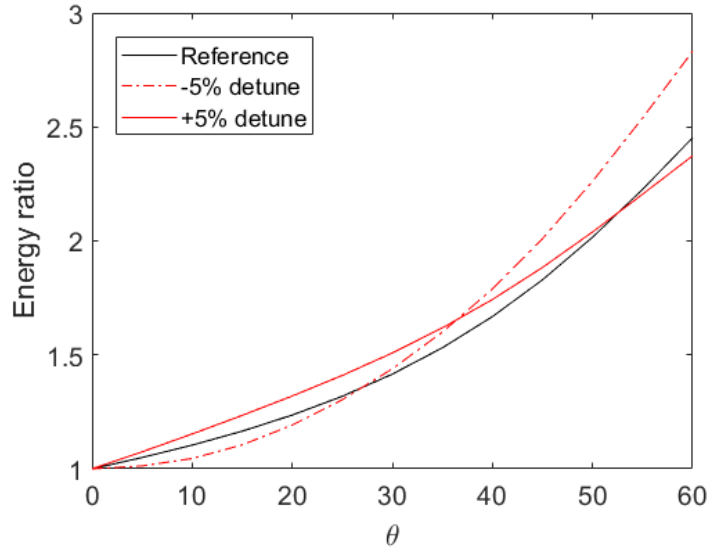


Fig. S18 Energy ratio of two nanowires as a function of incident angle (θ) for TM polarization and 550 nm incident light. Black solid line is for two identical nanowires. Red solid (dashed) line is when the nanowire's widths are different by 5%. The same type of monotonic relation between the energy ratio and incident angle is obtained. After a proper calibration, they are essentially equally effective in angle sensing.

Section 11. The non-monotonicity of photocurrent ratio for the TE polarization

In our experiment, the photocurrent ratio between the nanowires for the TE polarized illumination increases monotonically up to 45° (Fig. 4f). This non-monotonicity is the direct result of the radiation patterns of the superradiant and subradiant eigenstates. Here we will discuss it in detail.

The radiation patterns of the superradiant and subradiant eigenstates are determined by the spacing between the nanowires. The radiation pattern shown in Fig. S2 only applies when the spacing is much smaller than wavelength. As the spacing increases, the radiation pattern becomes more complex with multiple peaks in a number of directions. For the case considered in Fig. 4f of the main text, we plot the radiation patterns of the eigenstates in Fig. S19 for the structure used in our experiment. The gap between the nanowires is 100 nm and the operation wavelength is 550 nm.

The angular response is monotonic up to 45° . As can be seen in Fig. S19a, the excitation amplitude of the superradiant eigenstate decrease quickly beyond 45° . Only the subradiant eigenstate is excited. As a result, the contrast ratio between the wires, created by the interference between the superradiant and subradiant eigenstates, decreases as the incident angle increases beyond 45° .

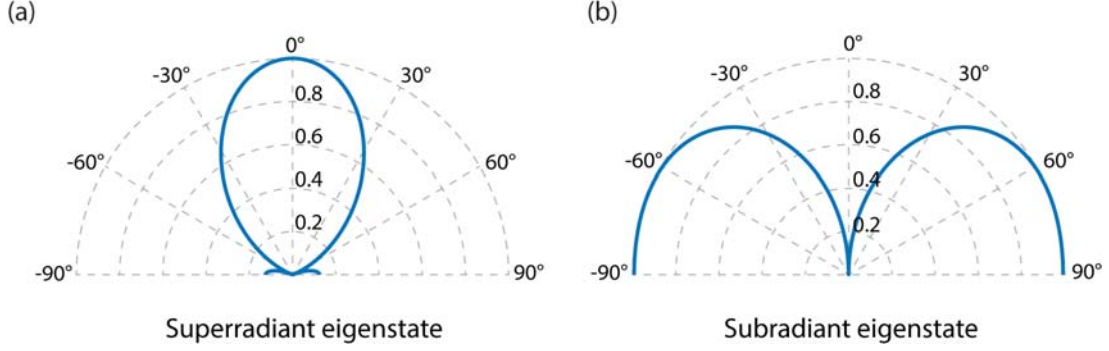


Fig. S19 Radiation pattern of eigenstates. (a)-(b) Angular profile (blue curve) and the phase configuration of the radiation of the superradiant eigenstate (a) and subradiant eigenstate (b) for the case of TE modes in our experiment. The gap between the nanowires (100 nm) is comparable to the operation wavelength (550 nm).

Section 12. The experimental error bars of triangulation.

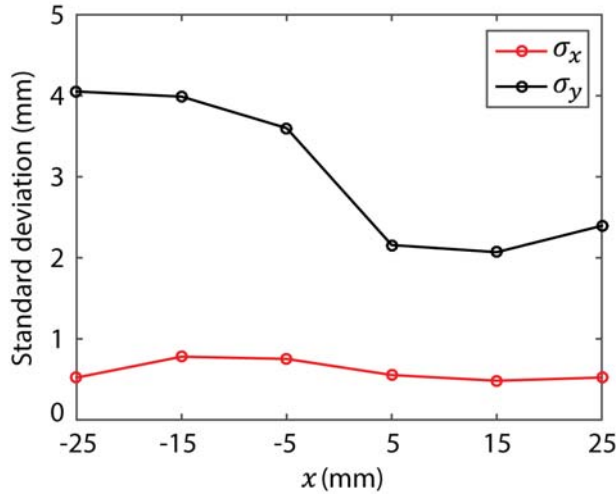


Fig. S20 Standard deviation in x - (σ_x) and y -direction (σ_y) for 6 different LED position measurements using a setup as shown in Fig. 5a. σ_x and σ_y corresponds to the length of error bars in Fig. 5b.

Using triangulation, the location of the LED during movement in Fig. 5b, including both the lateral position x and the depth y can be obtained from the measured incident angles $\Theta_{1,2}$ for the LED light falling onto the two angle sensors:

$$(x, y) = \left(\frac{(\tan\Theta_1)x_1 - (\tan\Theta_2)x_2}{\tan\Theta_1 - \tan\Theta_2}, \frac{\tan\Theta_1 \cdot \tan\Theta_2}{\tan\Theta_1 - \tan\Theta_2} \cdot (x_1 - x_2) \right) \quad (\text{S29})$$

where $x_{1,2}$ are the coordinates of the two detectors. Θ in Eq. S29 is defined with respect to horizontal plane i.e. $\Theta = 90^\circ$ for normal incidence.

In the experiment, we moved the position of the LED from (-25, 100) to (25, 100) in a 10 mm increment along the x -direction, corresponding to 6 different LED positions. Fifty measurement samples were collected on each angle-sensing photodetector for each LED position. Propagation

of uncertainty [23] was used to calculate the uncertainty i.e. standard deviation in the x - and y -direction as shown in Fig. S20 which corresponds to the length of error bars in Fig. 5b. The uncertainty in the x -direction (σ_x) remains less than 1 mm for the entire measurement whereas in the y -direction, σ_y is higher than in the x -direction. The lateral accuracy is better than the depth. In order to focus the LED light through the chopper, we placed a small reflector behind LED that caused anisotropic radiation, which has resulted in a relatively high σ_y when the LED was on the left side. Nevertheless, our angle-sensing photodetector has an accuracy in the mm range for a light source located 10 cm away and can precisely perform a lens-less positioning.

Section 13. Measurement resolution for angle and depth sensing

Assuming a photodetector operating with 43.4 dB signal-to-noise ratio (SNR) as in Ref [24], here we calculate the accuracy for depth sensing around the direction of the substrate normal.

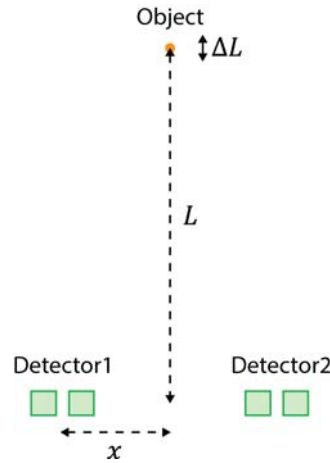


Fig. S21 Schematic of depth sensing using two angle-sensing detectors. The distance between two detectors is $2x$. L is the distance from the object to the center point between the two detectors. ΔL is the depth resolution.

If we define the distance between the object and the center point between two detectors as L , and the distance between two detectors as $2x$, depth resolution ΔL can be expressed as

$$\Delta L = x \sec^2 \theta \Delta \theta \quad (S30)$$

where $\theta = \text{atan}\left(\frac{L}{x}\right)$. For instance, when $L=10$ m and $x=10$ cm, ΔL is only 15.7 cm which quite accurate relative to the distance. Here, we used $\Delta \theta = 0.009^\circ$ which is acquired from Eq. S36.

Section 14. Derivation of the minimum detectable angle change $\delta\theta$.

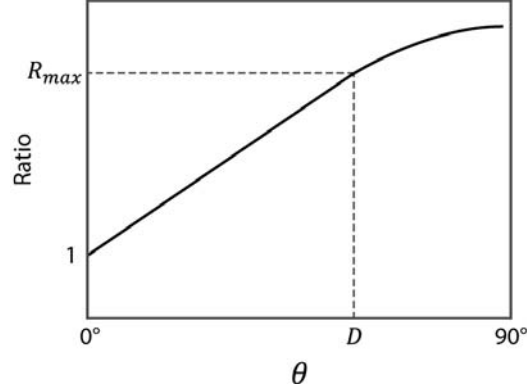


Fig. S22 An example of a contrast ratio of photocurrent having a linear response up to D degree.

The angular accuracy for the two-wire detector system $\delta\theta$ can be expressed as:

$$\delta\theta = \Delta R \cdot \frac{d\theta}{dR} \quad (\text{S31})$$

where R is the contrast ratio. Assuming a linear angular dependence as in Fig. S22, $d\theta/dR$ can be expressed as

$$\frac{d\theta}{dR} = \frac{D}{R_{max} - 1} \quad (\text{S32})$$

where D is the dynamic range of the incident angle and R_{max} is the maximum contrast ratio at D degree.

Now we calculate the accuracy for incident light around normal direction. Since $R = I_1/I_2$ where I_1 and I_2 are the photocurrent in two nanowires, ΔR can be expressed as:

$$\Delta R = \left| \frac{dR}{dI_1} \right| \Delta I_1 + \left| \frac{dR}{dI_2} \right| \Delta I_2 = \left| \frac{1}{I_2} \right| \Delta I_1 + \left| \frac{I_1}{I_2^2} \right| \Delta I_2 \quad (\text{S33})$$

Since $I_1 \approx I_2$ for normal incident direction, the equation above can be simplified as

$$\Delta R = \left| \frac{1}{I_1} \right| \Delta I_1 + \left| \frac{1}{I_2} \right| \Delta I_2 = \frac{2}{SNR} \quad (\text{S34})$$

Thus, substituting Eq. S32 and S34 into Eq. S31, we get

$$\delta\theta = \frac{2}{SNR} \cdot \frac{D}{R_{max} - 1} \quad (\text{S35})$$

Assuming $SNR = 43.4dB$ and using $R_{max} = 1.3$ and $D = 30^\circ$ which is based on our experimental results in Fig. 5c, $\delta\theta$ can be calculated as

$$\delta\theta = \frac{2}{10^{4.34}} \cdot \frac{30^\circ}{1.3 - 1} \approx 0.009^\circ \quad (\text{S36})$$

Section 15. 3D angle sensing analysis.

A single angle-sensing detector can only detect the incident angle of light in 2D space. In 3D space, single detector cannot be used to detect the incident angle of light since both polar θ and azimuthal ϕ angles need to be determined. For example, let us assume incident angle $\theta = \phi = 45^\circ$. Light with this incident angle will generate a well-defined photocurrent ratio. However, there are multiple incident angles that can generate the same photocurrent ratio. This is shown in Fig. S23a where all the directions that generate the same photocurrent ratio as $\theta = \phi = 45^\circ$ are lighted up with yellow color. Here, the purple spherical grid with a 5 degree mesh resolution is used to visualize the 3D space surrounding the angle sensor. We can place another detector next to the original detector but rotating 90° . This second detector will also have a photocurrent ratio and there will be multiple directions that generate the same amount of photocurrent ratio which is shown in Fig. S23b. Thus, the true incident angle of light can be determined (limiting the detection region to either top or bottom hemisphere) by overlapping the yellow regions in Fig. S23a and Fig. S23b.

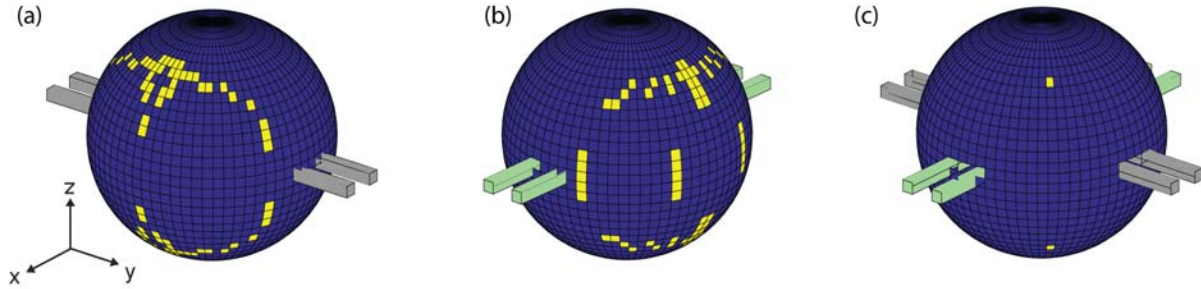


Fig. S23 3D angle sensing of unpolarized light with 550 nm wavelength using two detectors. (a) Purple grid with 5 degree mesh resolution is used to represent the 3D space. Yellow regions indicate the possible incident angle directions since the same photocurrent ratio as $\theta = \phi = 45^\circ$ is obtained. (b) Similar to (a) but with the detector that is rotated 90 degrees. (c) By overlapping yellow regions in (a) and (b), the true incident angle can be determined. Two detectors do not actually overlap. It is only for drawing purpose. They are placed next to each other in real world.

Section 16. The limit of the spacing between nearby angle sensing pixels.

The optical cross section of the nanowires can be very large due to the optical resonances supported the wires. Therefore, when angle sensing pixels are densely packed on a chip, there is a minimal spacing between pixels for the most optimal operation. When the spacing is smaller than the illumination wavelength, neighboring pixels can no longer be considered as being by themselves and the interaction between nearby pixels can reduce the accessible range for the angle sensing. Figure S24a shows an example of 300 nm spaced pixels, which has reduced dynamic range up to 25 degrees as shown in Fig. S24b. When the distance increases to 500 nm, the coupling effect become negligible.

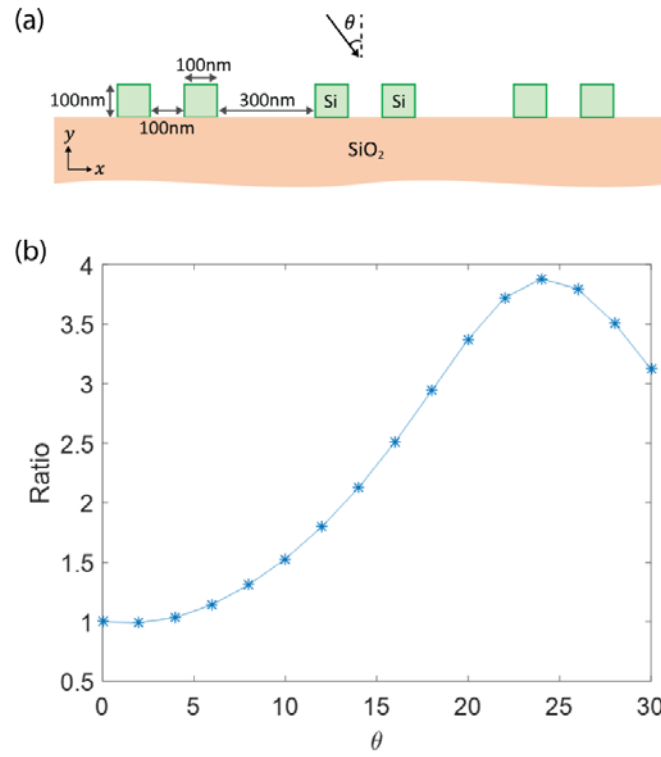


Fig. S24 Array of angle-sensing detectors. (a) Schematic of three detectors placed next to each other with 300nm gap. (b) Energy ratio of two nanowires in single pixel under incident light having 580 nm wavelength.

References

- [1] Suh, W., Wang, Z. & Fan, S. Temporal coupled-mode theory and the presence of non-orthogonal modes in lossless multimode cavities. *IEEE J. Quantum Electron.* **40**, 1511–1518 (2004).
- [2] Verslegers, L., Yu, Z., Catrysse, P. B. & Fan, S. Temporal coupled-mode theory for resonant apertures. *Journal of the Optical Society of America B* **27**, 1947 (2010).
- [3] Verslegers, L., Yu, Z., Ruan, Z., Catrysse, P. B. & Fan, S. From electromagnetically induced transparency to superscattering with a single structure: A coupled-mode theory for doubly resonant structures. *Phys. Rev. Lett.* **108**, 83902 (2012).
- [4] Maksimov, D. N., Sadreev, A. F., Lyapina, A. A. & Pilipchuk, A. S. Coupled mode theory for acoustic resonators. *Wave Motion* **56**, 52–66 (2015).
- [5] Scully, M. O. Collective Lamb Shift in Single Photon Dicke Superradiance. *Phys. Rev. Lett.* **102**, 143601 (2009).
- [6] Zhang, S. *et al.* Anti-Hermitian Plasmon Coupling of an Array of Gold Thin-Film Antennas for Controlling Light at the Nanoscale. *Phys. Rev. Lett.* **109**, 193902 (2012).
- [7] Dicke, R. H. Coherence in Spontaneous Radiation Processes. *Phys. Rev.* **93**, 99–110 (1954).
- [8] Lyuboshitz, V. L. Resonance Interaction between Two Identical Dipole Emitters, Soviet Physics JETP, **26**, 937-942 (1968)
- [9] Makhmetov, G. E., Borisov, A. G., Teillet-Billy, D. & Gauyacq, J. P. Interaction Between Overlapping Quasi-Stationary States: He(2 1 S and 2 1 P) Levels in Front of an Aluminium Surface. *EPL Europhys. Lett.* **27**, 247 (1994).
- [10] Okołowicz, J., Płoszajczak, M. & Rotter, I. Dynamics of quantum systems embedded in a continuum. *Phys. Rep.* **374**, 271–383 (2003).
- [11] Suh, W., Wang, Z. & Fan, S. Temporal coupled-mode theory and the presence of non-orthogonal modes in lossless multimode cavities. *IEEE J. Quantum Electron.* **40**, 1511–1518 (2004).
- [12] Verslegers, L., Yu, Z., Catrysse, P. B. & Fan, S. Temporal coupled-mode theory for resonant apertures. *Journal of the Optical Society of America B* **27**, 1947 (2010).
- [13] Verslegers, L., Yu, Z., Ruan, Z., Catrysse, P. B. & Fan, S. From electromagnetically induced transparency to superscattering with a single structure: A coupled-mode theory for doubly resonant structures. *Phys. Rev. Lett.* **108**, 83902 (2012).
- [14] Scully, M. O. Collective Lamb Shift in Single Photon Dicke Superradiance. *Phys. Rev. Lett.* **102**, 143601 (2009).
- [15] Zhang, S. *et al.* Anti-Hermitian Plasmon Coupling of an Array of Gold Thin-Film Antennas for Controlling Light at the Nanoscale. *Phys. Rev. Lett.* **109**, 193902 (2012).
- [16] Yariv, A., Xu, Y., Lee, R. K. & Scherer, A. Coupled-resonator optical waveguide: a proposal and analysis. *Opt. Lett.* **24**, 711–713 (1999).

- [17] Maksimov, D. N., Sadreev, A. F., Lyapina, A. A. & Pilipchuk, A. S. Coupled mode theory for acoustic resonators. *Wave Motion* **56**, 52–66 (2015).
- [18] Podolskiy, V. A., Sarychev, A. K., Narimanov, E. E. & Shalaev, V. M. Resonant light interaction with plasmonic nanowire systems. *J. Opt. Pure Appl. Opt.* **7**, S32 (2005).
- [19] Behdad, N., Al-Joumayly, M. & Li, M. Biomimetic electrically small antennas. *Electron. Lett.* **46**, 1650–1651 (2010).
- [20] Ellis, R. E., Adcock, F. Improvements in Means for Determining the Direction of a Distant Source of Electro-magnetic Radiation. British patent 130,490, Aug 7 (1919).
- [21] Green, T. C., Guion, W. G., Travers, D. N. & Sherrill, W. M. Quadrupole adcock direction finder and antenna therefor. U.S. patent 3,939,477, Feb 17 (1976).
- [22] Kim, S. J., Fan, P., Kang, J.-H. & Brongersma, M. L. Creating semiconductor metafilms with designer absorption spectra. *Nat. Commun.* **6**, 7591 (2015).
- [23] Taylor, J. R. An Introduction to Error Analysis, 2nd Edition (University Science Books, Sausalito, 1997).
- [24] ON Semiconductor, NOIV1SN025KA - VITA 25K Image Sensor Data Sheet, 2016 Rev.10, <http://www.onsemi.com/pub/Collateral/NOIV1SN025KA-D.PDF>